

Nitrogen hydrides in interstellar gas

II. Analysis of *Herschel**/HIFI observations towards W49N and G10.6–0.4 (W31C)

C.M. Persson¹, M. De Luca², B. Mookerjee³, A.O.H. Olofsson¹, J.H. Black¹, M. Gerin², E. Herbst⁴, T.A. Bell⁵,
A. Coutens^{6,7}, B. Godard⁵, J.R. Goicoechea⁵, G.E. Hassel⁸, P. Hily-Blant⁹, K.M. Menten¹⁰, H.S.P. Müller¹¹,
J.C. Pearson¹², S. Yu¹²

¹ Chalmers University of Technology, Department of Earth and Space Sciences, Onsala Space Observatory, SE-439 92 Onsala, Sweden. e-mail: carina.persson@chalmers.se

² LERMA-LRA, UMR 8112 du CNRS, Observatoire de Paris, École Normale Supérieure, UPMC & UCP, 24 rue Lhomond, 75231 Paris Cedex 05, France

³ Tata Institute of Fundamental Research, Homi Bhabha Road, Mumbai 400005, India

⁴ Department of Chemistry, University of Virginia, McCormick Road, Charlottesville, VA 22904, USA

⁵ Centro de Astrobiología, CSIC-INTA, 28850, Madrid, Spain

⁶ Université de Toulouse, UPS-OMP, Toulouse, France

⁷ CNRS, IRAP, 9 Av. Colonel Roche, BP 44346, F-31028 Toulouse Cedex 4, France

⁸ Department of Physics & Astronomy, Siena College, Loudonville, NY 12211, USA

⁹ Laboratoire d'Astrophysique de Grenoble, UMR 5571-CNRS, Université Joseph Fourier, Grenoble, France

¹⁰ Max-Planck-Institut für Radioastronomie, Auf dem Hügel 69, D-53121 Bonn, Germany

¹¹ I. Physikalisches Institut, Universität zu Köln, Zùlpicher Str. 77, 50937 Köln, Germany

¹² Jet Propulsion Laboratory, California Institute of Technology, 4800 Oak Grove Dr., Pasadena CA 91109, USA

Received Dec 20, 2011 / Accepted May 30, 2012

ABSTRACT

As a part of the *Herschel* key programme PRISMAS, we have used the *Herschel*-HIFI instrument to observe interstellar nitrogen hydrides along the sight-lines towards eight high-mass star-forming regions in order to elucidate the production pathways leading to nitrogen-bearing species in diffuse gas. Here, we report observations towards W49N of the NH $N=1-0$, $J=2-1$, and $J=1-0$, ortho-NH₂ $N_{K_a, K_c} J=1_{1,1} 3/2-0_{0,0} 1/2$, ortho-NH₃ $J_K=1_0-0_0$ and 2_0-1_0 , para-NH₃ $J_K=2_1-1_1$ transitions, and unsuccessful searches for NH⁺. All detections show absorption by foreground material over a wide range of velocities, as well as absorption associated directly with the hot-core source itself. As in the previously published observations towards G10.6–0.4, the NH, NH₂ and NH₃ spectra towards W49N show strikingly similar and non-saturated absorption features. We decompose the absorption of the foreground material towards W49N into different velocity components in order to investigate whether the relative abundances vary among the velocity components, and, in addition, we re-analyse the absorption lines towards G10.6–0.4 in the same manner. Abundances, with respect to molecular hydrogen, in each velocity component are estimated using CH, which is found to correlate with H₂ in the solar neighbourhood diffuse gas. The analysis points to a co-existence of the nitrogen hydrides in diffuse or translucent interstellar gas with a high molecular fraction. Towards both sources, we find that NH is always at least as abundant as both o-NH₂ and o-NH₃, in sharp contrast to previous results for dark clouds. We find relatively constant $N(\text{NH})/N(\text{o-NH}_3)$ and $N(\text{o-NH}_2)/N(\text{o-NH}_3)$ ratios with mean values of 3.2 and 1.9 towards W49N, and 5.4 and 2.2 towards G10.6–0.4, respectively. The mean abundance of o-NH₃ is $\sim 2 \times 10^{-9}$ towards both sources. The nitrogen hydrides also show linear correlations with CN and HNC towards both sources, and looser correlations with CH. The upper limits on the NH⁺ abundance indicate column densities $\lesssim 2-14\%$ of $N(\text{NH})$, which is in contrast to the behaviour of the abundances of CH⁺ and OH⁺ relative to the values determined for the corresponding neutrals CH and OH. Surprisingly low values of the ammonia ortho-to-para ratio are found in both sources, $\approx 0.5-0.7 \pm 0.1$, in the strongest absorption components. This result cannot be explained by current models as we had expected to find a value of unity or higher.

Key words. ISM: abundances – ISM: molecules – Sub-millimetre: ISM – Molecular processes – Line: formation – Astrochemistry

1. Introduction

Nitrogen is among the six most abundant elements in the universe and, despite its fundamental role in the chemistry of molecules connected with life, the chemical network of nitrogen in the interstellar medium is still poorly understood due to severe difficulties to observe key molecules from the ground.

Send offprint requests to: carina.persson@chalmers.se

* *Herschel* is an ESA space observatory with science instruments provided by European-led Principal Investigator consortia and with important participation from NASA.

Today about 55 molecules containing nitrogen have been discovered in interstellar space and a few more in circumstellar envelopes¹. The major reservoir of nitrogen is believed to be in the form of atomic N and molecular N₂. The latter is extremely difficult to observe since it has no permanent dipole moment (Sandford et al. 2001). In dense molecular clouds N₂H⁺ is instead often used as a tracer of N₂, which remained undetected until Knauth et al. (2004) reported far-ultraviolet observations towards HD 124314. The total abundance of nitrogen therefore

¹ www.astrochymist.org, www.astro.uni-koeln.de/cdms/molecules

still relies, to a high degree, on chemical modelling and observations of nitrogen-bearing species other than N_2 .

In order to constrain the nitrogen formation pathways, observations of *nitrogen hydrides* are crucial since they are at the root of the nitrogen chemical network, appearing in its first steps in chains of reactions that lead to other more complex species. The abundances of these species are thus key diagnostics for the nitrogen chemistry. The nitrogen hydrides are, however, also problematic to observe since their ground state rotational transitions lie at sub-mm wavelengths and are thus very difficult, or impossible, to reach from the ground. Key species, such as imidogen (NH) and amidogen (NH_2), have therefore previously not been widely observed, and there is still no detection of the NH^+ radical.

Although very few observations exist of NH and NH_2 in interstellar space, they are well known in comets (e.g. Swings et al. 1941; Meier et al. 1998; Feldman et al. 1993), and have been observed in stellar photospheres (e.g. Schmitt 1969; Farmer & Norton 1989) via their electronic, vibration-rotation, and high rotational transitions. The first detection of interstellar NH was made by Meyer & Roth (1991) by optical absorption spectroscopy. Subsequent observations by Crawford & Williams (1997) and Weselak et al. (2009) have yielded several lines of sight in diffuse and translucent gas where column densities of NH, CH, CN, and H_2 have been directly measured. The average value of the column density ratio in these diffuse and translucent sight-lines is $N(NH)/N(H_2) = 3 \times 10^{-9}$.

Interstellar NH_2 was first detected by van Dishoeck et al. (1993) in absorption towards Sgr B2 in three fine-structure components of the para-symmetry form of NH_2 , the $N_{K_a, K_c} = 1_{1,0} - 1_{0,1}$ transition, with partially resolved hyperfine structure at frequencies 461 to 469 GHz. The Infrared Space Observatory (ISO) was later used to observe unresolved absorption lines of both ortho and para symmetry forms of NH_2 , as well as NH, towards this source through the use of the long-wavelength spectrometer (Cernicharo et al. 2000; Goicoechea et al. 2004; Polehampton et al. 2007).

In contrast to NH and NH_2 , ammonia (NH_3) has been extensively observed for more than 40 years and was in fact the first polyatomic molecule to be identified in interstellar space (Cheung et al. 1968) by means of its $J = K$ inversion transitions at cm wavelengths (K is the quantum number of the projection of total angular momentum J on the molecule's symmetry axis). The ammonia molecule has, however, two symmetries, like NH_2 , which arise due to the possible orientations of the hydrogen spins and behave like two distinct species: ortho- NH_3 (all H spins parallel, $K = 3n$ where n is an integer ≥ 0) and para- NH_3 (not all H spins parallel, $K \neq 3n$). Important information about the ammonia formation pathways could be inferred from observations of both symmetries. Unfortunately, only the para form has relatively low-excitation transitions accessible from ground since the $K = 0$ ladder of energy levels has no inversion splitting and the $J_K = 3_3$ inversion transitions' lower energy level is 122 K above ground. Ortho inversion lines ($K = 3n$, $n \geq 1$) can thus only be observed in relatively warm molecular gas. Only a few ammonia observations of the cold diffuse interstellar gas exist, using para inversion lines (Nash 1990; Tieftrunk et al. 1994; Liszt et al. 2006) which leaves the ammonia formation mechanism poorly constrained in diffuse gas. The (0,0) ammonia ground state, with ortho symmetry, can only be studied by sub-mm rotational transitions. Observations of the fundamental rotational transition of ortho- NH_3 $J_K = 1_0 - 0_0$ at 572 GHz, which has similar upper state energy as the inversion lines, but several orders of magnitudes higher critical

densities, thus requires space telescopes. The Kuiper Airborne Observatory (Keene et al. 1983) performed the first observations of the $J_K = 1_0 - 0_0$ transition using heterodyne receivers, and later on the Odin satellite continued such observations in a number of environments, for instance in photo-dissociation and star-forming regions (e.g. Larsson et al. 2003; Persson et al. 2009), circumstellar envelopes (Hasegawa et al. 2006), diffuse clouds in absorption towards Sgr B2 (Wirström et al. 2010), and in comets (Biver et al. 2007).

With the launch of the *Herschel* Space Observatory (Pilbratt et al. 2010) in May 2009, unique opportunities to perform observations of transitions between 157 and 625 μm (0.48–1.9 THz) became feasible with the Heterodyne Instrument for the Far-Infrared (HIFI; de Graauw et al. 2010) owing to its very high sensitivity and spectral resolution. This allowed, for the first time, searches for spectrally resolved, rotational transitions involving the ground states of NH^+ , NH, NH_2 , and NH_3 with the same instrument. Several observations have already been reported. For instance, using *Herschel*-HIFI, Bacmann et al. (2010) found very high column densities of NH and ND in the cold envelope of the class 0 protostar IRAS16293-2422 ($2 \times 10^{14} \text{ cm}^{-2}$ and $\sim 1.3 \times 10^{14} \text{ cm}^{-2}$, respectively). Hily-Blant et al. (2010) found $NH:NH_2:NH_3$ abundance ratios of $\sim 5:1:300$ towards the same source.

The PRISMAS² key programme (PRobing InterStellar Molecules with Absorption line Studies) is targeting absorption lines in the line-of-sight towards eight bright sub-millimetre-wave continuum sources using *Herschel*-HIFI: G10.6–0.4 (W31C), W49N, W51, G34.3+0.1, DR21(OH), SgrA (+ 50 km s^{-1} cloud), G005.9-0.4 (W28A) and W33A. High-resolution absorption line spectroscopy is generally a very sensitive and model-independent method for measuring column densities of interstellar molecules, and a powerful tool to probe the diffuse interstellar gas clouds with no or little excitation.

The first results and analysis of absorption lines of nitrogen hydrides along the sight-line towards the massive star-forming region G10.6–0.4 (W31C) have already been presented in Persson et al. (2010, hereafter paper I). Similar abundances with respect to the total amount of hydrogen $N_H = 2N(H_2) + N(H)$, were found for all three species: approximately 6×10^{-9} , 3×10^{-9} , and 3×10^{-9} for NH, NH_2 , and NH_3 , respectively. They were estimated across the whole line-of-sight and using the high temperature ortho-to-para limits of three and one for NH_2 and NH_3 , respectively. NH^+ was not detected at a 1σ rms level of 74 mK with a resolution of 1.1 MHz. The abundance patterns that we see in diffuse molecular gas are thus clearly very different from those in IRAS16293-2422 and Sgr B2, where $NH:NH_2:NH_3 \sim 1:10:100$ and the fractional abundance of NH is a few times 10^{-9} . The Sgr B2 results may, however, not be representative of cold dark clouds since this source is very complex and atypical.

The unexpectedly high NH abundance has been difficult to explain with chemical models and both the NH and NH_2 production by purely gas-phase processes is inhibited by a lack of a sufficient source of N^+ . The models fail to simultaneously predict the absolute and relative abundances of the nitrogen hydrides. Typical steady state *dark cloud* models ($n = 1 \times 10^3 - 5 \times 10^4 \text{ cm}^{-3}$, $T = 10 - 40 \text{ K}$, $A_V \gtrsim 10$), predict an NH_2 abundance of $(1-10) \times 10^{-8}$, an NH abundance 10 times lower, and an NH_2/NH_3 ratio of 0.3–1.5 for a wide range of assumptions (e.g. Langer & Graedel 1989; Millar et al. 1991), but these are not directly applicable to diffuse molecular gas. Examples of chem-

² <http://astro.ens.fr/?PRISMAS>

Table 1: Observed transitions towards W49N and G10.6–0.4.

Species	Frequency ^a (GHz)	Transition	Band ^b	T_{sys}^c (K)	t_{int}^d		T_C^e		$1\sigma/T_C^f$	
					G10.6 (s)	W49N (s)	G10.6 (K)	W49N (K)	G10.6	W49N
NH ^g	946.476	$N_J = 1_0 \leftarrow 0_1$	3b	416	234	116	2.5	3.4	0.021	0.027
	974.478	$N_J = 1_2 \leftarrow 0_1$	4a	338	186	103	2.6	3.9	0.018	0.018
o-NH ₂ ^h	952.578	$N_{K_a, K_c} J = 1_{1,1} 3/2 \leftarrow 0_{0,0} 1/2$	3b	230	92	68	2.6	3.6	0.018	0.017
o-NH ₃ ⁱ	572.498	$J_K = 1_0 \leftarrow 0_0$	1b	87	1 024	94	0.61	0.93	0.013	0.025
	1 214.859	$J_K = 2_0 \leftarrow 1_0$	5a	1 024	293	196	3.4	5.2	0.032	0.025
p-NH ₃	1 215.246	$J_K = 2_1 \leftarrow 1_1$	5a	1 024	293	196	3.4	5.2	0.032	0.025
NH ⁺	1 012.540	${}^2\Pi_{1/2} N = 1 \leftarrow 1 J = 3/2 \leftarrow 1/2$	4a	327	171	91	3.0	4.4	0.013	0.013

Notes. ^(a) The frequencies refer to the strongest hyperfine structure components. ^(b) HIFI consists of 7 different mixer bands and two double sideband spectrometers. All transitions were observed in the upper sideband except NH⁺. ^(c) System temperature. ^(d) The averaged on-source integration time for each transition. ^(e) The single sideband (SSB) continuum intensity (the observed double sideband (DSB) continuum divided by two). ^(f) The rms noise, at a resolution of 1.1 MHz, divided by T_C . ^(g) The quantum numbers for the rotational transition N_J are $F_1 = I_H + J$ and $F = I_N + F_N$ (Klaus et al. 1997). ^(h) The quantum numbers for the rotational transition $N_{K_a, K_c} J$ are $F_1 = I_N + J$ and $F = I_H + F_1$ (Müller et al. 1999). ⁽ⁱ⁾ The rotational energy is given by the two principal quantum numbers (J, K), corresponding to the total angular momentum and its projection along the molecular axis (e.g. Ho & Townes 1983; Rist et al. 1993).

ical models for diffuse cloud conditions are found in Fig. A.1 and A.2 in paper I. These models were also unable to explain the observed abundances and ratios. Processes on dust grains have previously been proposed as a way to increase the NH production (Meyer & Roth 1991; Wagenblast et al. 1993). Such models, however, often predict up to 1 000 times more NH₃ than NH₂ (Hasegawa & Herbst 1993, paper I). The importance of grain surface chemistry in diffuse clouds is also not clear since water ice mantles have not been detected in diffuse gas, and strong (UV) radiation fields counteract molecular formation on grains. Grain surface production of NH is therefore still debated, and would, if true, change our understanding of surface chemistry in diffuse gas. On the other hand, if grains indeed were unimportant in diffuse gas nitrogen chemistry it would imply that either key gas-phase reactions must have been overlooked, or that the uncertainty of some reaction rates could make a difference. Both additional high-quality observations and chemical modelling are needed to solve this problem.

In this paper, we present new observations and analyses of absorption lines in the line-of-sight towards the high-mass star-forming region W49N, and, we also re-analyse the absorption towards G10.6–0.4 in more detail. W49N is one of the most luminous high-mass star-forming regions in the Galaxy ($\sim 10^7 L_\odot$) with a core that contains more than a dozen ultra-compact H II regions (Dreher et al. 1984; Dickel & Goss 1990; De Pree et al. 2000). It is located on the far side of the Galaxy at a distance of 11.4 kpc with Galactic coordinates $l = 43.17^\circ$ and $b = 0.012^\circ$, in one of the most massive giant molecular clouds ($\sim 10^6 M_\odot$) in the Milky Way. The source velocity is about $+8 \text{ km s}^{-1}$ and the foreground gas along the line-of-sight is detected at $v_{\text{LSR}} \approx 30 - 75 \text{ km s}^{-1}$, revealing gas at two locations in the near and far side of the Sagittarius spiral arm around 40 and 60 km s^{-1} (Dame & Thaddeus 1985). The ultra-compact H II region G10.6–0.4 in the star-forming W31 complex is an extremely luminous sub-millimetre and infrared continuum source. The source is located within the so-called 30 km s^{-1} arm at a kinematic distance of 4.8 kpc (Fish et al. 2003). The gas associated directly with G10.6–0.4 is detected at a systemic source velocity of $v_{\text{LSR}} \approx -1 \text{ km s}^{-1}$, determined from OH maser emission observations, while the foreground gas is detected at $v_{\text{LSR}} \approx 10 - 55 \text{ km s}^{-1}$.

Section 2 summarises the observations and data reduction, and the results from our *Herschel* observations are found in Sect. 3. The hyperfine structure (hfs) components of the nitrogen hydrides are discussed in Sect. 4. In Sect. 5 we use three different methods to decompose the absorption lines along the sight-lines towards both sources in different velocity components, and estimate column densities, N , and relative abundances, X , in each component. We also compare the column densities of the nitrogen hydrides, both with each other to investigate possible correlations, and with other species tracing regions with both low and high molecular fractions. Section 6 presents our estimates of the ortho-to-para ratio (OPR) of NH₃. We end this paper with a summary and outlook in Sect. 7. Note that the analysis of the *background* source emissions and absorptions is left for a future paper.

2. Observations and data reduction

All the reported observations are a part of the more extended PRISMAS programme towards G10.6–0.4 and W49N. The nitrogen observations, which took place between March 2 and April 18, 2010, are summarised in Table 1. All *Herschel* identification numbers (OBSID's) are found in Table A.1 (on-line material). Note that NH $N_J = 1_0 - 0_1$ was observed together with CH₂ at 946 GHz, and ortho-NH₃ $J_K = 2_0 - 1_0$ was observed together with para-NH₃ $J_K = 2_1 - 1_1$ (the absorptions from the source are 97 km s^{-1} apart). Before the launch of *Herschel*, no observations of these NH₃ transitions, nor the NH⁺ ${}^2\Pi_{1/2} J = 3/2 \leftarrow 1/2$ transition, had been performed. We do not, however, analyse the ortho-NH₃ $J_K = 2_0 - 1_0$ transition in this paper since this line shows absorption only at the background source velocities.

We used the dual beam switch mode and the wide band spectrometer (WBS) with a bandwidth of 4×1 GHz and an effective spectral resolution of 1.1 MHz. The corresponding velocity resolution is about 0.3 km s^{-1} at the highest frequencies and 0.6 km s^{-1} at 572 GHz. In addition, simultaneous observations were performed using the high resolution spectrometer (HRS) with an effective spectral resolution of 0.25 MHz ($\Delta v \sim 0.1 \text{ km s}^{-1}$) and a bandwidth of 240–340 MHz except for the 1 214 and 1 215 GHz lines which had an effective resolution of 0.5 MHz ($\Delta v \sim 0.1 \text{ km s}^{-1}$) and a bandwidth of 780 MHz in

order to cover both lines in the same band. Note that the channel separation of the observations is 0.5 MHz in the WBS and 0.12 MHz in the HRS (0.24 MHz for the 1 215 GHz line). Each line was observed with three different frequency settings of the local oscillator (LO) corresponding to a change of approximately 15 km s^{-1} to determine the sideband origin of the lines. During all observations two orthogonal polarisations were used.

The pointings were centred at $\alpha = 19^{\text{h}}10^{\text{m}}13^{\text{s}}.2$, $\delta = 09^{\circ}06'12''$ (J2000) for W49N, and $\alpha = 18^{\text{h}}10^{\text{m}}28^{\text{s}}.7$, $\delta = -19^{\circ}55'5''$ (J2000) for G10.6–0.4. The recommended values for half-power beam width of the telescope are $44''.2$, $22''.1$, and $18''.9$ at 480, 960 and 1 120 GHz, respectively. The reference beams were located within $3'$ on either side of the source. The total calibration uncertainties are $\lesssim 9\%$ for band 1 and $\lesssim 13\%$ for band 5, including the sideband gain ratio uncertainty which is 3–4% for band 1b (ortho-NH₃), and 4–6% for band 5a (para-NH₃). All errors are added in quadrature. Detailed information about the HIFI calibration including beam efficiency, mixer sideband ratio, pointing, etc., can be found on the Herschel internet site³. The in-flight performance is described by Roelfsema et al. (2012). Since we are interested in absorption lines and their relative strength compared to the continuum in this paper, the forward efficiency of 96% and the main beam-efficiency of 64–76% (between 1 120 and 480 GHz) do not affect our results and we have therefore used a T_{A}^* intensity scale throughout this paper.

The data were processed using the standard *Herschel* Interactive Processing Environment (HIPE,⁴ Ott 2010), version 5.1, up to level 2 which provides fully calibrated spectra. The data quality is excellent with very low intensity ripples in most cases, typically below a few percent of the double sideband continuum. For NH⁺ in both sources and both polarisations, and o-NH₃ at 572 GHz in the vertical polarisation towards G10.6–0.4, we corrected the data from ripples using the *fitHifiFringe* tool in HIPE (in paper I we only used one polarisation for these two transitions). The FITS files were then exported to the spectral line software package *xs*⁵ which was used in the subsequent data reduction.

The two polarisations are generally in agreement to better than 10%. The three LO-tunings are also in very good agreements without contamination from the image sideband with one exception in W49N around the o-NH₃ at 572 GHz line (see Sect. 3.1.1). In all other spectra we averaged the three LO-tunings and both polarisations.

For the above line identification work we used the Cologne Database for Molecular Spectroscopy⁶ (CDMS, Müller et al. 2005), the Jet Propulsion Laboratory catalogue⁷ (JPL, Pickett et al. 1998), and Frank Lovas' Spectral Line Atlas of Interstellar Molecules⁸ (SLAIM). Laboratory measurements of NH transitions have been performed by e.g. Klaus et al. (1997) and Flores-Mijangos et al. (2004), and measurements of o-NH₂ by e.g. Müller et al. (1999). A review on ammonia is found in Ho & Townes (1983), and an investigation of the hyperfine structure

components of ortho-NH₃ at 572 GHz was recently performed by Cazzoli et al. (2009). NH⁺ measurements have been made by Verhoeve et al. (1986) and Hübbers et al. (2009).

3. Observational results

Figures 1 and G.1 (on-line material) show the averaged double sideband WBS spectra of the transitions listed in Table 1 towards W49N and G10.6–0.4, respectively (special treatment of o-NH₃ 1₀–0₀ in W49N is found in Sect. 3.1.1). All detected species show very similar absorption patterns over a wide range of velocities, although W49N has fewer absorbing velocity components in the line-of-sight. No detections of NH⁺ have been found in any of the two sources.

The resulting noise and single sideband (SSB) continuum levels, for each transition, are found in Table 1. Note that since HIFI uses double side band (DSB) receivers, the observed continuum has to be divided by two to obtain the SSB continuum. The sideband gain ratio is assumed to be unity throughout this paper. This has proven to be a good assumption based on PRISMAS observations of saturated absorption lines like HF that establish the true zero levels (Neufeld et al. 2010b).

3.1. Background source emission

Even though we only analyse the absorption lines in the foreground clouds in this paper we still have to take the source emission into account in the analysis. Several spectra show broad emission features from the background sources which extend far into the velocity range pertaining to the line-of-sight clouds.

Ammonia in particular shows strong emission at the background source velocities with self-absorption around +13 and 0 km s⁻¹ for W49N and G10.6–0.4, respectively. A large part of the NH 974 GHz emission at the source velocities in both sources is most likely not from NH, but from HCN $J = 11 - 10$ at 974.487 GHz, only 9 MHz above the NH line corresponding to 2.5 km s^{-1} . The PRISMAS observations of these sources have detected three additional HCN emission lines: $J = 6 - 5$ at 532 GHz, $J = 7 - 6$ at 620 GHz, and $J = 10 - 9$ at 886 GHz which strengthens our identification. In addition, we detect no NH emission in the 946 GHz transition which is a further confirmation that the emission is due to another species. HCN in foreground gas is unlikely to produce measurable absorption in the $J = 11 - 10$ transition because the excitation energy of the lower state, $E_{10}/k = 234 \text{ K}$, is much too high to be populated at the density and temperature of diffuse or translucent gas.

In the analysis performed in Sect. 5 using three different methods, we have removed the broad emission lines that overlap with the absorption in the line-of-sight by means of Gaussian fits.

3.1.1. Emission line contamination

In W49N, close to the o-NH₃ line at 572 GHz, an emission line from the lower sideband, identified as the $J_{K_a, K_c} = 16_{6,10} - 16_{5,11}$ SO₂ line, moves across the ammonia absorption lines in the different LO-tunings. Thus for the o-NH₃ 572 GHz transition in W49N we were only able to use the A and C LO-settings in Table A.1, which also had to be cut to remove the parts contaminated by the SO₂ line.

The o-NH₂ absorption towards W49N is contaminated by an emission line in the same sideband from the source. We identify the emission line as a blend of three unresolved hfs compo-

³ <http://herschel.esac.esa.int/Docs/HIFI/html/ch5.html>

⁴ HIPE is a joint development by the *Herschel* Science Ground Segment Consortium, consisting of ESA, the NASA *Herschel* Science Centre, and the HIFI, PACS and SPIRE consortia.

⁵ Developed by Per Bergman at Onsala Space Observatory, Sweden; <http://www.chalmers.se/rss/oso-en/observations/data-reduction-software>

⁶ <http://www.cdms.de>

⁷ <http://spec.jpl.nasa.gov>

⁸ <http://physics.nist.gov/>

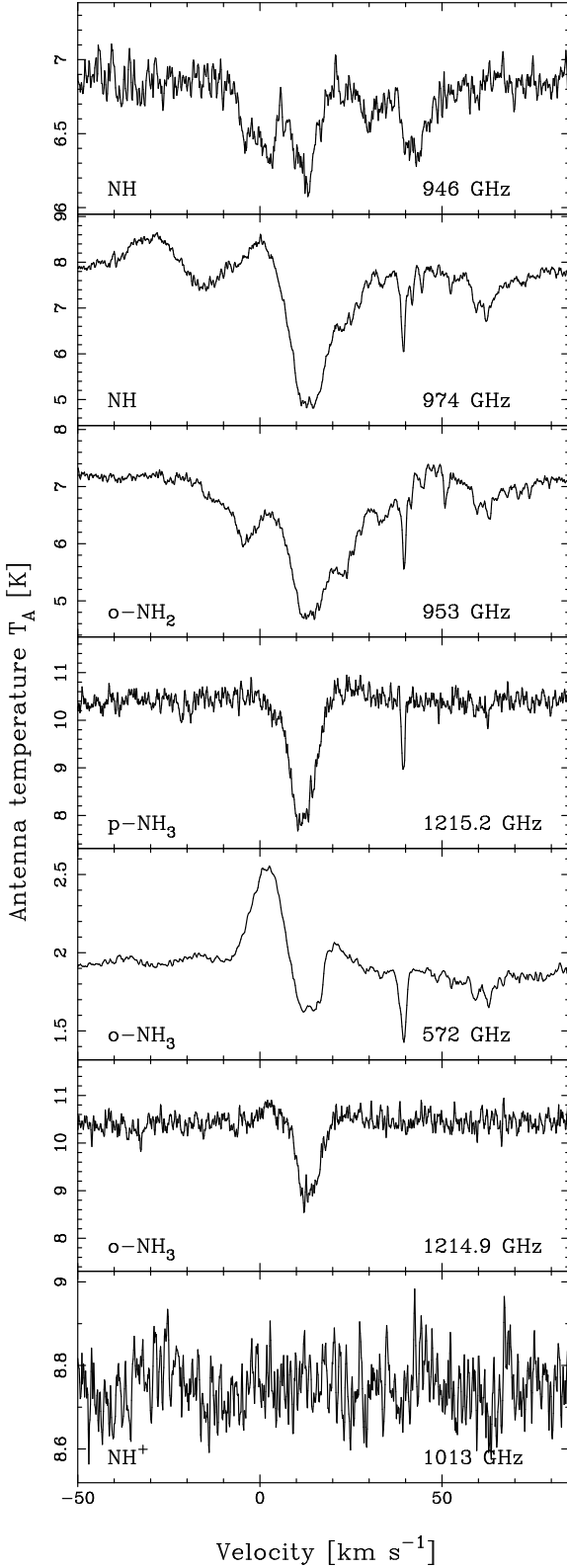


Fig. 1: *Nitrogen hydrides towards W49N*: Double sideband WBS spectra of NH, ortho-NH₂, ortho- and para-NH₃, and NH⁺ over the LSR velocity range -50 to 85 km s⁻¹. Quantum numbers are found in Table 1. Note that we only analyse the absorption in the velocity range 30–75 km s⁻¹ in this paper and leave the source absorption and emission for a future paper.

nents of NO ${}^2\Pi_{1/2} J = 9.5^f \rightarrow 8.5^f$, $F = 10.5-9.5, 9.5-8.5$, and $8.5-9.5$, at 952.464201 GHz. The NO emission line is removed from the o-NH₂ absorption (described in Sect. B, on-line material), and in all following figures in this paper we show o-NH₂ in W49N with removed NO emission. The NO identification is strengthened by the PRISMAS observations of three additional NO lines towards W49N shown in Fig. B.2 (on-line material). No emission of NO is found towards G10.6–0.4.

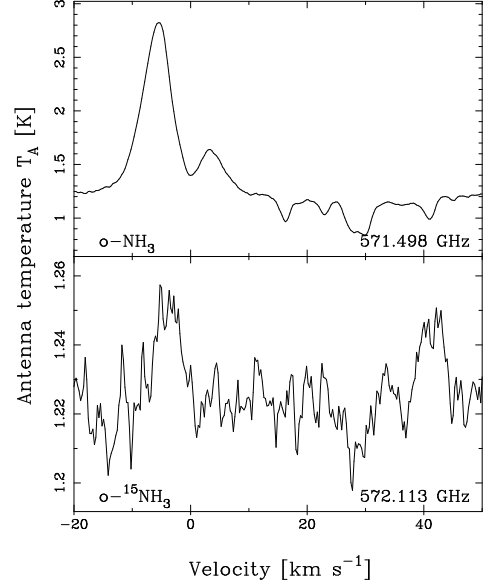


Fig. 2: *W31C: o-¹⁴NH₃ and o-¹⁵NH₃*. Both isotopologues show emission from the source. Absorption in the line-of-sight is only seen in the o-¹⁴NH₃ spectra. The emission line at $v_{\text{LSR}} \approx 41$ km s⁻¹ in the o-¹⁵NH₃ spectra, is an SO₂ line from the upper sideband.

3.1.2. The ¹⁵NH₃ isotopologue: only in G10.6–0.4

Since our observations also covered the frequency of o-¹⁵NH₃ $J_K = 1_0-0_0$ at 572.113 GHz, we have checked the averaged spectra for emission and/or absorption features of this isotopologue. In Figs. 2 and G.2 (on-line material) we show a 5σ emission feature in G10.6–0.4 with an amplitude of 40 mK and a line-width of about 4 km s⁻¹, which we identify as o-¹⁵NH₃ 1_0-0_0 , giving a source velocity of ~ -4 km s⁻¹. Checking the possibility of absorption lines of o-¹⁵NH₃ in the line-of-sight towards G10.6–0.4, we note that there seems to be an absorption feature corresponding to the strongest velocity components of o-¹⁴NH₃ at $\sim 27-32$ km s⁻¹. This feature is, however, probably not a real detection since it would otherwise imply that ${}^{14}\text{N}/{}^{15}\text{N} \sim 20$. This is about 20 times lower than the ${}^{14}\text{N}/{}^{15}\text{N}$ ratio in the local ISM which is about ~ 450 (Wilson & Rood 1994), or 441 ± 5 in the Solar nebula (Marty et al. 2011). Odin observations of absorption towards Sgr B2 show ${}^{14}\text{NH}_3/{}^{15}\text{NH}_3 > 600$ (Wirström et al. 2010). Lower ratios have been found, for instance, in low mass cores, 334 ± 50 (Lis et al. 2010), and on Earth, ~ 270 . Adande & Ziurys (2011) find values of $\sim 100-350$ using CN and HNC in ten dense molecular clouds located at various galactic distances from the Galactic Centre, but this is still several times higher than inferred from a possible o-¹⁵NH₃ absorption. The ${}^{14}\text{N}/{}^{15}\text{N}$ ratio is also difficult to determine and the results using cyanides may differ from the ratio inferred from other

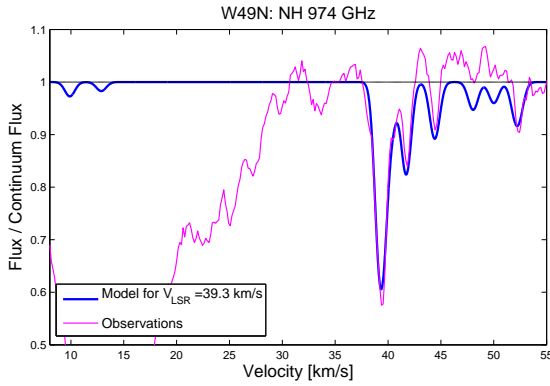


Fig. 3: *NH* hfs components: Normalised WBS spectrum towards W49N. Also shown are Gaussian fits with a line width of 1 km s^{-1} of the NH 974 GHz hfs components in the $+39 \text{ km s}^{-1}$ velocity component.

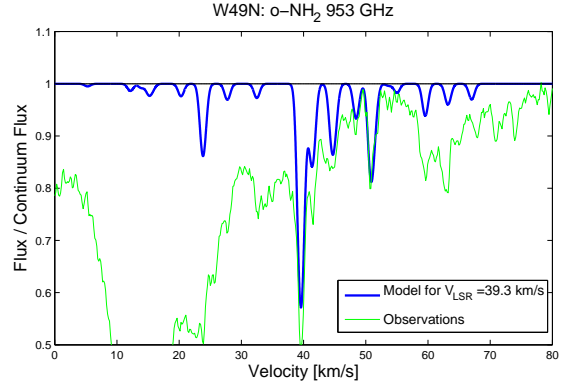


Fig. 4: *Ortho-NH₂* hfs components: Normalised WBS spectrum towards W49N. Also shown are Gaussian fits with a line width of 1 km s^{-1} of the o-NH₂ 953 GHz hfs components in the $+39 \text{ km s}^{-1}$ velocity component.

species such as N_2H^+ , and may not reflect the true $^{14}\text{N}/^{15}\text{N}$ abundance ratio. More observations are needed to lower the noise in order to obtain a real detection of $^{15}\text{NH}_3$ and to determine the true $^{14}\text{N}/^{15}\text{N}$ ratio towards G10.6–0.4.

In W49N, no o- $^{15}\text{NH}_3$ detection is made due to blending SO_2 lines from the upper sideband which are both stronger and broader than in G10.6–0.4. In addition, the o- $^{14}\text{NH}_3$ emission is more than two times weaker than in G10.6–0.4, and the spectrum has a three times higher noise level which does not allow a detection of o- $^{15}\text{NH}_3$ emission from the source.

4. Hyperfine structure components

Both NH and NH_2 have numerous hyperfine structure (hfs) components which require a high resolution spectrometer, such as HIFI, to be spectrally resolved. The on-line Tables C.1–C.3 list the hfs components of the NH 974 and 946 GHz, and the o-NH₂ 953 GHz transitions which have 21, 9, and 30 hfs components, respectively. The observed NH 974 GHz and o-NH₂ transitions in the $+39 \text{ km s}^{-1}$ velocity component towards W49N are shown in Figs. 3 and 4 together with models of respective transition, including hfs components, using Gaussian opacity profiles and a line width of 1 km s^{-1} . Here, the intensities have been normalised to the continuum in single sideband as $T_A/T_C - 1$ assuming a sideband gain ratio of unity where T_A is the observed intensity and T_C is the SSB continuum as measured in line-free regions in the spectra. The large number of hfs components, in addition to many different, overlapping, velocity components in the line-of-sight, complicates the analysis substantially. In particular, the o-NH₂ hfs components in the line-of-sight absorption overlap with the source emission/absorption, thus requiring a source model in the analysis.

The much simpler hyperfine structure of the ortho- and para-NH₃ ground state rotational transitions has never been resolved in space before *Herschel*. The Odin satellite was able to observe the 572 GHz ammonia transition, but the velocity resolution of about 0.5 km s^{-1} was not enough to spectrally resolve the hfs components even though the asymmetric line shapes hinted the hfs components (e.g. Liseau et al. 2003). Figure 5 shows an example of our observations of the 572 GHz o-NH₃ transition in the $+39 \text{ km s}^{-1}$ absorption velocity component towards W49N with the HRS and a velocity resolution of 0.13 km s^{-1} . Three hfs components are seen at 38.4, 39.4 and 40.0 km s^{-1} although the line width of 1.0 km s^{-1} prevents a detailed check of the

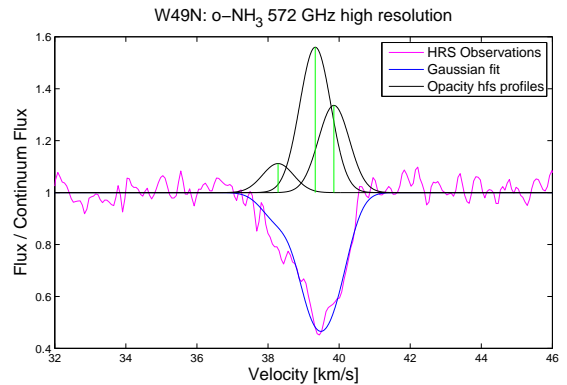


Fig. 5: *Ortho-NH₃* hfs components: Normalised high resolution spectra ($\Delta v = 0.13 \text{ km s}^{-1}$) towards W49N in the $+39 \text{ km s}^{-1}$ velocity component. Three hfs components are seen at 38.4, 39.4 and 40.0 km s^{-1} . Also shown are the positions and relative intensities of the hfs components and their fitted opacity profiles with a line width of 1.0 km s^{-1} .

relative intensities. In the Gaussian fit we therefore use 0.2, 1 and 0.6 as relative intensities, with corresponding relative offsets at $-1.05, 0.0,$ and 0.52 km s^{-1} found by Cazoli et al. (2009) (Table C.4, on-line material). The positions and relative intensities of the hfs components and the fitted opacity profiles are also shown in Fig. 5. The six hfs components in the para-NH₃ line at 1 215 GHz are even more closely spaced and not resolved (Table C.5).

The WBS ammonia observations do not spectrally resolve the NH₃ hfs components ($\Delta v = 0.6 \text{ km s}^{-1}$ at 572 GHz and $\Delta v = 0.3 \text{ km s}^{-1}$ at 1 215 GHz), but we still take the hfs components into account in the following NH₃ modelling since they produce a slightly asymmetric line shape and a systematic line broadening.

5. Analysis: Velocity decomposition, column densities, and abundances

In paper I we estimated the abundances towards G10.6–0.4 simply by evaluating the integrated opacity of each line over the velocity range $11 - 54 \text{ km s}^{-1}$. This approach gave a first estimate

of the average abundance in the full line-of-sight, but did not take into account possible abundance variations in the different velocity components. In addition, no source model was included, and thus the blend of the NH and o-NH₂ hfs components from the foreground absorptions with the source absorption was neglected.

In this paper we use three different approaches to decompose the absorption into separate velocity components, and to obtain column densities and abundances in each component. Each method has its own strengths and weaknesses, and differences in the results can be considered an estimate of the errors of the methods. If all three methods point to the same result, it will be considered as robust. We note, however, that the uncertainties of the data are higher towards W49N than for G10.6–0.4, since we have removed a SO₂ line from the upper sideband in the ortho-NH₃ absorption, and an NO line in the o-NH₂ absorption.

In this work we also only estimate N and X for the ortho-symmetries of NH₂ and NH₃ since our own measurements of the ammonia OPR in Sect. 6 do not point to the high temperature limit, but instead suggest an OPR *lower* than unity, which cannot be straightforwardly explained. If this unexpected low ammonia OPR is true, then the processes that affect the ammonia OPR perhaps also could affect the OPR of NH₂ in diffuse clouds about which we have no information. And since we want to compare relative abundances, we choose to focus on the ortho-symmetries since both are observed in NH₂ and NH₃, and also since the o-NH₃ observations have higher S/N than the p-NH₃.

To obtain integrated opacities of each transition, in each velocity component, the first method uses Gaussian fitting (Sect. 5.2), while the second one uses the observed spectra of ortho-NH₃ and CH as templates for other species (Sect. 5.3). Both methods calculate the opacity as $\tau = -\ln(T_A/T_C - 1)$. The derived integrated opacities are then used to estimate column densities by means of the non-LTE (Local Thermodynamic Equilibrium) RADEX code (Sect. 5.1). As a third method, we have used XCLASS (Sect. 5.4) which, in contrast to RADEX, assumes fixed excitation temperatures, to obtain column densities in each velocity component directly.

In order to be able to use our results as comparisons with chemical models, we need to derive the abundance of the species with respect to the total amount of gas. The difficulty is to obtain reliable estimates of $N(\text{H})$ and/or $N(\text{H}_2)$. In paper I, we compared the nitrogen hydrides column densities to the total amount of hydrogen in the line-of-sight, $N_{\text{H}} = N(\text{H}) + 2N(\text{H}_2)$. This can not be done in the present work since the neutral hydrogen absorption shows too broad and overlapping absorption components over much larger velocity ranges as compared to the nitrogen hydrides. In order to estimate the amount of molecular hydrogen in each (narrow) velocity component, we therefore consider the comparison with CH (Gerin et al. 2010b) as an abundance determination. This can be made using the CH/H₂ correlation ($\text{CH}/\text{H}_2 = 3.5 \times 10^{-8}$) observed by Sheffer et al. (2008) in the solar neighbourhood diffuse medium. This correlation is assumed to be valid in regions which are dominated by ultraviolet radiation where $N(\text{CH}) \lesssim 2 \times 10^{14} \text{ cm}^{-2}$. In this way we can use our own PRISMAS observations of CH and measure abundance ratios obtained with the same instrument.

The physical properties of the bulk of the absorbing gas in our sight-lines are (Gerin et al. 2010b), according to the definitions of Snow & McCall (2006), a mixture of diffuse ($N_{\text{H}} \lesssim 500 \text{ cm}^{-3}$ and $A_{\text{v}} \lesssim 1$) and translucent gas ($500 \lesssim N_{\text{H}} \lesssim 5000 \text{ cm}^{-3}$ and a shielding $1 \lesssim A_{\text{v}} \lesssim 5$). And since the comparison later in this section of the nitrogen hydrides with other species tracing both high and low density gas, points to an

existence in the denser parts of the gas, molecular hydrogen is most likely the dominant form of hydrogen in these components.

Assuming that the nitrogen hydrides co-exist with HF and H₂O in the line-of-sight material we use the fact that the saturated absorptions of the latter two species reach the zero level, for a sideband ratio of unity, to support our assumption that the foreground absorbing material completely covers the continuum within the beam. Comparison spectra of o-NH₃ and o-H₂O are shown in Figs. 8–9, and with HF, ortho- and para-H₂O in Figs. G.9–G.10 (on-line material).

Table 2: Conversion factors^a.

Species x	Transition (GHz)	T_{ex} (K)	$N(x) \int \tau dv = 1.0 \text{ km s}^{-1}$ (cm^{-2})	
NH	946.476	3.9	3.65×10^{13}	<i>a</i>
	974.478	4.0	7.47×10^{12}	<i>a</i>
o-NH ₂	952.578	3.9	3.62×10^{12}	<i>b</i>
o-NH ₃	572.498	2.8	3.92×10^{12}	<i>b</i>
p-NH ₃	1 215.245	4.9	1.65×10^{13}	<i>b</i>
NH ⁺	1 012.524	4.2	6.48×10^{12}	
CH	532.724	2.9	2.28×10^{13}	<i>b</i>
HNC	90.664	2.8	1.80×10^{12}	<i>b</i>
CN	113.169	2.8	1.90×10^{13}	<i>b</i>

Notes. ^(a) The excitation temperatures and conversion factors from integrated opacity, $\int \tau dv = 1.0 \text{ km s}^{-1}$, to column densities, $N(x)$, are calculated using RADEX with $T_{\text{k}} = 30 \text{ K}$ and $n(\text{H}_2) = 500 \text{ cm}^{-3}$ which corresponds to $n_{\text{H}} \gtrsim 10^3 \text{ cm}^{-3}$. ^(b) Integrated over all hfs components.

5.1. RADEX

Observations of absorption lines can provide accurate determinations of molecular column densities if the observed transitions trace all of the populated states. In the case of NH₃ we observe two transitions of the ortho (A-symmetry) form, arising in the $J_K = 0_0$ and 1_0 states, and one transition of the para (E-symmetry) form arising in the lower 1_1 rotation-inversion level. Although the upper 1_1 inversion level is less metastable than the lower one, it may still be significantly populated. The metastable 2_2 para levels and 3_3 ortho levels may also have significant populations in diffuse molecular clouds at low density, $n_{\text{H}} \lesssim 10^4 \text{ cm}^{-3}$, owing to infrared pumping and formation. Because we are directly sensitive to three lower states and lack direct information about the excitation temperatures of the observed transitions, we use the non-equilibrium RADEX code (van der Tak et al. 2007) to relate the total column density of ammonia to the observed integrated optical depths. The models provide integrated opacities of both observed and unobserved excited levels and quantify possible effects of stimulated emission, chemistry, and electron collisions. Results for one reference model are summarised in Table 2, where conversion factors for all nitrogen hydrides and comparison species are listed in terms of the total column density $N(x)$ of molecule x that is needed to achieve an integrated optical depth $\int \tau dv = 1.0 \text{ km s}^{-1}$ in the specified transition. In this model we treat ortho- and para-symmetries separately. The integrated optical depth is a sum over all hyperfine structure in the transition.

We have assumed diffuse molecular cloud conditions with a kinetic temperature of 30 K and a density of molecular hydrogen

$n(\text{H}_2) = 500 \text{ cm}^{-3}$, which corresponds to $n_H \gtrsim 10^3 \text{ cm}^{-3}$. The resulting conversion factors for the rotational ground state transitions are not very sensitive to density, temperature or electron collisions. The critical densities of the fundamental rotational transitions of NH, NH₂, and NH₃ are high, $n_{\text{crit}} \sim 10^8 \text{ cm}^{-3}$. This means the upper energy levels of these transitions must be excited almost entirely radiatively at the low densities in diffuse gas. We find, however, that electron collisions can be responsible for excitation temperatures of $\sim 4 \text{ K}$ in the cm-wave inversion transitions rather than $\lesssim 3 \text{ K}$ that would be found in conventional excitation analyses at low densities, $n(\text{H}_2) \lesssim 10^3 \text{ cm}^{-3}$. Where collision rates are unknown, we have made guesses scaled in proportion to radiative line strengths. The background radiation field includes both the 2.725 K cosmic microwave background and a model of the Galactic infrared radiation in the solar neighborhood. The resulting excitation temperatures of the observed sub-millimetre transitions are typically 3–4 K, which are small enough compared to $h\nu/k$ that no correction for emission is required. Note that the lower state of the 572 GHz transition contains 95% of the ortho molecules while the lower state of the 1215.2 GHz transition occupies only 43% of the para molecule.

5.2. Method I: Multi-Gaussian fit of the nitrogen hydrides simultaneously

We have modelled the observed spectra of NH, o-NH₂, and o-NH₃ using Gaussian optical depth profiles. These were generated for each hfs component of each species in separate velocity intervals, and were made to fit the observations under the condition that the LSR velocity and width in each velocity component must be the same for all molecules. This can be made assuming that all species co-exist in the same velocity ranges and therefore show absorption at the same velocities. This assumption is supported by the striking similarities of the strongest NH, o-NH₂ and o-NH₃ absorptions, despite the complicated hyperfine structure patterns of NH and o-NH₂, shown in normalised comparison spectra in Fig. G.9 (on-line material). We note that a good fit therefore is a good indicator if this assumption is valid.

The observed line profiles are thus modelled by Gaussian components of both the hfs components and all velocity components according to

$$\frac{T_A}{T_C} = \exp \left[- \sum_{i=1}^{N_v} \sum_{j=1}^{N_{\text{hfs}}} \tau_{\text{hfs}}(j) \tau_0(i) \exp \left[-4 \ln(2) \left(\frac{v - v_0(i) - v_{\text{hfs}}(j)}{\Delta v} \right)^2 \right] \right]$$

where N_v is the number of the modelled velocity components (same for all species), N_{hfs} is the number of hfs components (which differs between species), τ_{hfs} is the theoretical relative line strength of each hfs component, τ_0 is the opacity of the strongest hfs component in each velocity component, v_0 is the LSR velocity of each velocity component, v_{hfs} is the relative velocity offset of the hfs components with respect to the strongest, and Δv is the FWHM (full width of half maximum). We assume that $\tau_{\text{hfs}} = A_{ul} \times g_u / (A_{ul}(\text{main}) \times g_u(\text{main}))$ for the hfs components of NH and o-NH₂, since the many overlapping velocity components prevent a check of the relative intensities of these components.

We have used both ortho- and para-NH₃, which are not significantly complicated by hfs splitting, to determine the minimum number of velocity components needed, and also to set-up reasonable initial guesses for the line properties necessary for the fitting procedure to converge at all. The fitting was done for each velocity component at a time in a loop until all fits had converged. The fits are most likely not unique. Provided that the fits

are good and that we use the same velocity parameters for all species, this is, however, not considered important as we do not ascribe any physical meaning to the Gaussian components.

The results from Method I are peak opacities, line widths and centre velocities for each velocity component and species. The integrated opacity in each velocity component was assumed to be well represented by $\int \tau dv = 1.06 \Delta v \tau_{\text{peak}}$. The non-detections of NH⁺ are used to put upper limits on its integrated opacities (3σ). We then used the conversion factors in Table 2 to calculate the column densities tabulated in Table 3. Typical errors in the G10.6–0.4 resulting column densities for NH, o-NH₂ and o-NH₃ are between 7 and 15%. In the $v_{\text{LSR}} = 45 \text{ km s}^{-1}$ component, the errors are 22% for all three species, and 23% in the $v_{\text{LSR}} = 39 \text{ km s}^{-1}$ component for NH. The errors in W49N varies between 8 to 11% for all three species, except in the 33 km s^{-1} component where the uncertainties are 37, 26 and 31% for NH, o-NH₂ and o-NH₃, respectively. The errors include calibration uncertainties (see Sect. 6) as well as uncertainties from the fitting procedure.

In addition to the nitrogen hydrides, we also modelled the PRISMAS CH 532 GHz transition, and the CN 113 GHz and HNC 91 GHz transitions observed with the IRAM 30 m antenna (Godard et al. 2010). These species were not included in the fitting procedure described above. Instead we have used the resulting velocity parameters from the fits of the nitrogen hydrides (v_{LSR} and line widths) since we want to investigate possible correlations and make abundance determinations only in the same parts of velocity space as the nitrogen hydrides. The resulting CH column densities are found in Table 3, and the CN and HNC column densities in the on-line Table F.1.

Figures 6 and 7 show the fits and residuals of the nitrogen hydrides together with CH. The resulting fits are well reproducing the observations for all species except for CH suggesting that CH exist in a more widely spread gas than the nitrogen hydrides.

The CH column densities are then used together with the relation $[\text{CH}]/[\text{H}_2] = 3.5 \times 10^{-8}$ (Sheffer et al. 2008) to estimate the abundances listed in Table 3.

5.3. Method II: ortho-NH₃ and CH as templates for other species

This method directly compares the opacity line profile of the non-saturated o-NH₃ line at 572 GHz with the line profiles of NH and o-NH₂, convolved with respective hyperfine structure. This assumes that all species co-exist in the same velocity ranges, and that the opacity ratios depend only on their column density ratios, which may vary from one velocity component to another. No opacity profile is assumed for a given absorbing cloud so, unlike what is done by methods I and III, we do not attempt to decompose the velocity structure of the template line into a number of Gaussian curves. We perform, instead, simple cuts of the template profile into large velocity bins.

The hfs of the o-NH₃ line is not resolved in the WBS data and introduces only a small broadening of the lines that is dealt with by smoothing the NH and o-NH₂ spectra. Before comparing the opacity profiles, we mask out those portions of the spectra where a simple scaling between template and target is not expected, such as the velocity range associated to the background sources, and remove the emission line wing by Gaussian fitting. We note that the removal of the line wing introduces very large uncertainties towards W49N around 33 km s^{-1} where a weak absorption component is visible. This method therefore disregards the results in this velocity component.

Table 3: *Method I results^a*.

W49N												
v_{LSR} (km s ⁻¹)	Δv (km s ⁻¹)	$N(\text{NH})$ (cm ⁻²)	$N(\text{oNH}_2)$ (cm ⁻²)	$N(\text{oNH}_3)$ (cm ⁻²)	$N(\text{NH}^+)$ (cm ⁻²)	$N(\text{CH})$ (cm ⁻²)	$\frac{\text{NH}}{\text{oNH}_3}$	$\frac{\text{oNH}_2}{\text{oNH}_3}$	$X(\text{NH})^b$	$X(\text{oNH}_2)^b$	$X(\text{oNH}_3)^b$	$X(\text{NH}^+)^b$
33.3	2.1	1.5e12	2.1e12	4.6e11	$\lesssim 3.3\text{e}11$	1.6e13	3.3	4.6	3.3e-9	4.6e-9	1.0e-9	$\lesssim 7.2\text{e}-10$
39.5	1.1	1.0e13	7.3e12	4.3e12	$\lesssim 2.4\text{e}11$	2.3e13	2.3	1.7	1.5e-8	1.1e-8	6.5e-9	$\lesssim 3.7\text{e}-10$
59.2	2.9	9.2e12	4.1e12	2.1e12	$\lesssim 7.5\text{e}11$	6.0e13	4.4	2.0	5.4e-9	2.4e-9	1.2e-9	$\lesssim 4.4\text{e}-10$
62.7	2.3	8.0e12	3.9e12	2.2e12	$\lesssim 6.3\text{e}11$	5.1e13	3.6	1.8	5.5e-9	2.7e-9	1.5e-9	$\lesssim 4.3\text{e}-10$
Total:	...	2.9e13	1.7e13	9.1e12	$\lesssim 2.0\text{e}12$	1.5e14	3.2	1.9	6.7e-9	4.1e-9	2.1e-9	$\lesssim 4.6\text{e}-10$
Mean:	...	7.2e12	4.4e12	2.3e12	$\lesssim 4.9\text{e}11$	3.8e13	3.2	1.9	6.7e-9	4.1e-9	2.1e-9	$\lesssim 4.6\text{e}-10$
Median:	...	8.6e12	4.0e12	2.2e12	$\lesssim 4.8\text{e}11$	3.7e13	4.0	1.9	8.1e-9	3.8e-9	2.0e-9	$\lesssim 4.5\text{e}-10$
G10.6–0.4												
v_{LSR} (km s ⁻¹)	Δv (km s ⁻¹)	$N(\text{NH})$ (cm ⁻²)	$N(\text{oNH}_2)$ (cm ⁻²)	$N(\text{oNH}_3)$ (cm ⁻²)	$N(\text{NH}^+)$ (cm ⁻²)	$N(\text{CH})$ (cm ⁻²)	$\frac{\text{NH}}{\text{oNH}_3}$	$\frac{\text{oNH}_2}{\text{oNH}_3}$	$X(\text{NH})^b$	$X(\text{oNH}_2)^b$	$X(\text{oNH}_3)^b$	$X(\text{NH}^+)^b$
16.2	1.7	2.0e13	9.6e12	4.2e12	$\lesssim 4.7\text{e}11$	5.8e13	4.8	2.3	1.2e-8	5.8e-9	2.5e-9	$\lesssim 2.8\text{e}-10$
18.8	1.5	6.1e12	3.1e12	8.7e11	$\lesssim 4.1\text{e}11$	2.6e13	7.0	3.6	8.2e-9	4.2e-9	1.2e-9	$\lesssim 5.5\text{e}-10$
22.1	4.4	1.6e13	6.9e12	1.8e12	$\lesssim 1.2\text{e}12$	7.7e13	8.9	3.8	7.3e-9	3.1e-9	8.2e-10	$\lesssim 5.5\text{e}-10$
22.8	1.0	1.0e13	3.6e12	1.5e12	$\lesssim 2.7\text{e}11$	7.1e12	6.7	2.4	4.9e-8	1.8e-8	7.4e-9	$\lesssim 1.3\text{e}-9$
24.8	3.1	6.2e12	4.3e12	1.4e12	$\lesssim 8.4\text{e}11$	3.7e13	4.4	3.1	5.9e-9	4.1e-9	1.3e-9	$\lesssim 8.0\text{e}-10$
27.8	1.9	2.7e13	1.2e13	7.3e12	$\lesssim 5.0\text{e}11$	7.4e13	3.7	1.6	1.3e-8	5.7e-9	3.5e-9	$\lesssim 2.4\text{e}-10$
29.9	1.7	2.9e13	1.3e13	7.9e12	$\lesssim 4.6\text{e}11$	5.6e13	3.7	1.6	1.8e-8	8.1e-9	4.9e-9	$\lesssim 2.9\text{e}-10$
32.1	1.5	9.0e12	3.5e12	1.3e12	$\lesssim 4.1\text{e}11$	3.5e13	6.9	2.7	9.0e-9	3.5e-9	1.3e-9	$\lesssim 4.1\text{e}-10$
36.1	4.0	2.0e13	6.5e12	3.2e12	$\lesssim 1.1\text{e}12$	7.8e13	6.3	2.0	9.0e-9	2.9e-9	1.4e-9	$\lesssim 4.9\text{e}-10$
39.0	1.2	1.1e13	3.0e12	4.7e11	$\lesssim 3.1\text{e}11$	3.3e13	23	6.4	1.2e-8	3.2e-9	5.0e-10	$\lesssim 3.3\text{e}-10$
40.9	1.7	3.0e13	1.1e13	4.1e12	$\lesssim 4.7\text{e}11$	5.4e13	7.3	2.7	1.9e-8	7.1e-9	2.7e-9	$\lesssim 3.0\text{e}-10$
45.0	1.4	3.0e12	1.1e12	5.9e11	$\lesssim 3.6\text{e}11$	1.1e13	5.1	1.9	9.6e-9	3.5e-9	1.9e-9	$\lesssim 1.1\text{e}-9$
Total:	...	1.9e14	7.8e13	3.5e13	$\lesssim 6.8\text{e}12$	5.5e14	5.4	2.2	1.2e-8	5.0e-9	2.2e-9	$\lesssim 4.4\text{e}-10$
Mean:	...	1.6e13	6.5e12	2.9e12	$\lesssim 5.7\text{e}11$	4.6e13	5.4	2.2	1.2e-8	5.0e-9	2.2e-9	$\lesssim 4.4\text{e}-10$
Median:	...	1.4e13	5.4e12	1.7e12	$\lesssim 4.7\text{e}11$	4.6e13	8.2	3.3	1.0e-8	4.2e-9	1.3e-9	$\lesssim 3.6\text{e}-10$

Notes. ^(a) LSR velocity, v_{LSR} , line width, Δv , column densities, $N(x)$, and abundances, $X(x) = N(x)/N(\text{H}_2)$, of each velocity component, including 3σ upper limits of $N(\text{NH}^+)$. Note that we estimate N and X only for the ortho-symmetry forms of NH_2 and NH_3 . ^(b) Using $[\text{CH}]/[\text{H}_2] = 3.5 \times 10^{-8}$ (Sheffer et al. 2008).

The velocity bins into which the o- NH_3 opacity profile is split are chosen to be significantly larger than the original resolution, but narrow enough to separate the most prominent velocity features (typically a few km s⁻¹, see Table D.1). Each velocity bin of the o- NH_3 template is then convolved, channel by channel, with the NH and o- NH_2 hfs components. We thus obtain an intermediate opacity model of how the NH and o- NH_2 spectra would appear if absorption were limited to the selected velocity bin. The observed o- NH_3 opacity is then fitted by the IDL Least Squares Fitting routine MPFIT (Markwardt 2009) with a linear combination of the intermediate models. The output of the fits consists of the opacity ratios, between the o- NH_3 and the modelled NH and o- NH_2 spectra, in the various velocity bins.

To obtain column densities in each velocity bin, we sum the opacities of all channels of the template transition, and then apply the RADEX conversion factors from Table 2. The resulting abundance ratios are finally used to obtain column densities of the other species. Typical errors (including both calibration and fitting uncertainties) are 5–15% except for the 43.5–50 km s⁻¹ velocity bin in G10.6–0.4 and the 50–57 km s⁻¹ velocity bin in W49N which both have an uncertainty of approximately 25%.

The main advantage of this method is that a small number of free parameters is needed to obtain a reasonable fit since it uses, as much as possible, the information carried by the template spectrum. The model also avoids the problem of non-

uniqueness of Gaussian decompositions of the absorption profiles and allows a straightforward comparison of column densities evaluated for exactly the same velocity intervals. On the other hand, such rigidity in the definition of the velocity bins does not allow us to reliably retrieve the column density ratios if the absorption comes from very different gas volumes resulting in significant velocity shifts of the absorption features between the two species. We note that the fit quality, estimated with $\int |\text{residuals}| \times dv / \int \tau \times dv$, is a good indicator of such cases. Note also that residual baseline structures, like those produced by standing waves or by an imperfect removal of ammonia emission line wings, may introduce artificial discrepancies between the template spectra and the modelled species.

In addition to the above modelling, we use the o- NH_3 as a template for CN and HNC (Godard et al. 2010), and also use the deconvolved CH spectrum at 532.724 GHz (Gerin et al. 2010b) as a template to model all three nitrogen hydrides, in order to obtain an estimate of the abundance with respect to molecular hydrogen.

The resulting column densities and relative abundances in different velocity bins are given in Table D.1, except for the CN and HNC results which are found in on-line Table F.2.

The model fits compared to the normalised spectra in both sources are shown in Figs. G.3–G.6 (on-line material). The fit

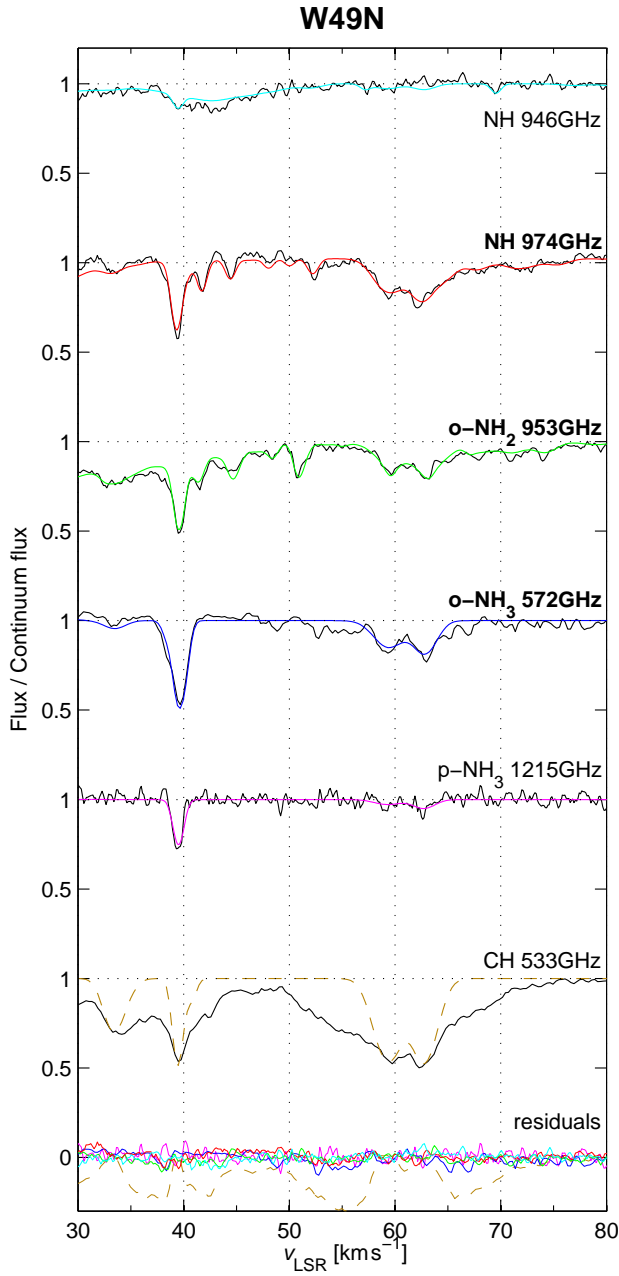


Fig. 6: *W49N*: Fits of Method I and the SSB normalised spectra of the nitrogen hydrides and CH. The black lines are the observations, and the coloured lines are the model fits. In the bottom the residuals are plotted on top of each other with respective colour. The three transitions used in Method I to determine the v_{LSR} and line widths of the velocity components are marked in bold.

qualities of the comparisons between the o-NH_3 , NH and o-NH_2 are excellent, except in the narrow and deep $+39 \text{ km s}^{-1}$ component towards *W49N* which was very difficult to model. The modelling of the nitrogen hydrides using CH as a template show on the other hand rather low fit qualities, suggesting that the assumption that the nitrogen hydrides and CH only come from the same gas is less justified, also supported by Method I.

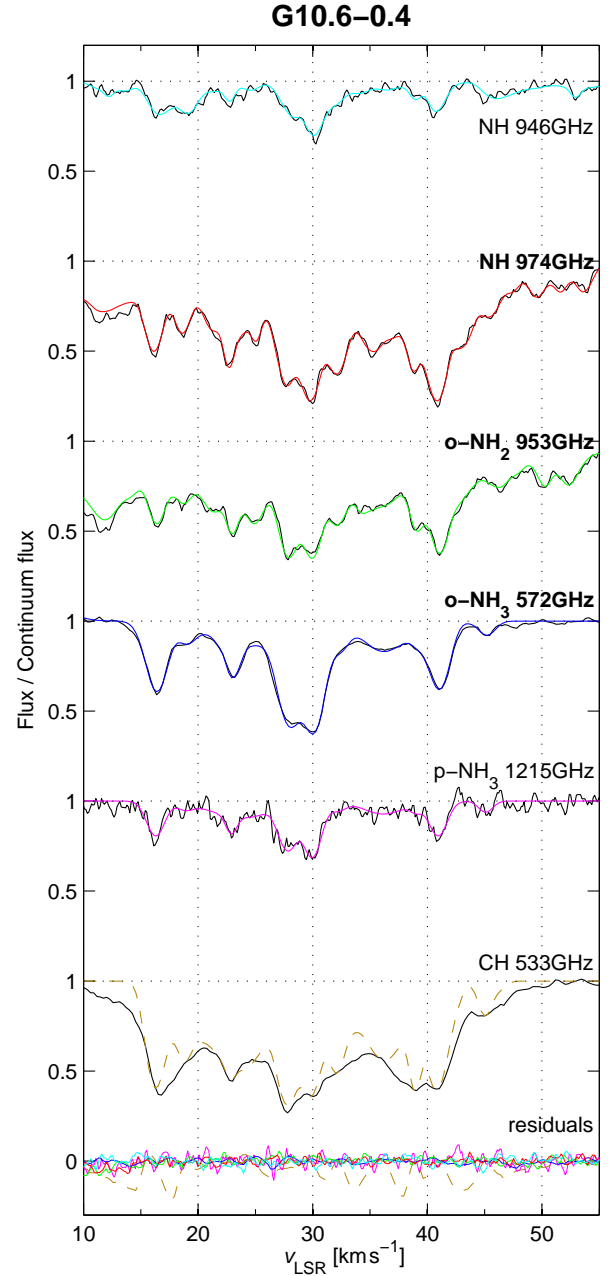


Fig. 7: *G10.6-0.4*: Fits of Method I and the SSB normalised spectra of the nitrogen hydrides and CH. Same notation as in Fig. 6.

5.4. Method III: XCLASS

Finally, we have generated synthetic spectra separately for NH, o-NH_2 , o-NH_3 , CH, CN, and HNC using the software XCLASS⁹ (created by P. Schilke, and described by Comito et al. 2005, and references therein) by considering for each species all hfs components and velocity components and the assumption of a fixed excitation temperature. The synthetic spectra generated with XCLASS were fitted to the observed spectra using MAGIX, an iterating engine that allows automatic minimization to constrain model parameters. XCLASS accesses the CDMS and JPL molecular databases, and models each molecule with the follow-

⁹ <https://www.astro.uni-koeln.de/projects/schilke/XCLASS>

ing free parameters: source size, temperature, column density, line width and velocity offset relative to the systemic velocity of the source, and derives the column density corresponding to the different velocity components detected in absorption and emission in the observed spectra. The source size refers to the relative size of the absorbing cloud vs. the continuum source, which is assumed to be fully covered within the beam. We have assumed a Gaussian profile for each hfs component, and an excitation temperature of 4 K. Since Method III explicitly assumes a fixed excitation temperature for the estimate of column densities, it is significantly different from methods I and II.

Figures G.7 and G.8, in the on-line material, show the model fits together with the observed SSB normalised spectra. Resulting column densities and abundance ratios of the nitrogen hydrides and CH are found in the on-line Table E.1, and the CN and HNC column densities in on-line Table F.1.

5.5. Comparison of results

The results from all three methods agree very well, especially considering that the velocity bins used are not the same.

The total $N(\text{CH})$ from all methods are lower than found by Gerin et al. (2010b), which is expected since we only use parts of the CH absorptions. Comparisons of CH in different velocity bins give much more similar results in both sources. Since we use CH as a tracer of H_2 , we also compare our estimate of $N(\text{H}_2)$ with Nyman & Millar (1989) towards W49N: for the $+39 \text{ km s}^{-1}$ component they suggest $N(\text{H}_2) = 3 \times 10^{21} \text{ cm}^{-2}$ and they also quote $N(^{13}\text{CO}) = 7 - 30 \times 10^{15} \text{ cm}^{-2}$ which gives $N(\text{H}_2) = 7 - 30 \times 10^{21} \text{ cm}^{-2}$ using a standard conversion factor of 10^{-6} . They also suggest column densities towards W49N between $50 - 70 \text{ km s}^{-1}$: $N(\text{H}_2) = 5 \times 10^{21} \text{ cm}^{-2}$ and $N(\text{H}_2) = 5.5 - 23 \times 10^{21} \text{ cm}^{-2}$ from ^{13}CO observations. All these suggestions for $N(\text{H}_2)$ are several times higher than inferred from our CH observations. This is, however, not surprising because the ^{13}CO conversion factor is rather uncertain at such low column densities. Plume et al. (2004) also obtain higher $N(\text{H}_2)$ than we do towards W49N. The total amount of $N(\text{H}_2)$ in the sight-lines towards our sources, can also be compared with estimates from the K-band extinction (Marshall et al. 2006): $N(\text{H}_2) = 1.3 \times 10^{22}$ and $7.5 \times 10^{21} \text{ cm}^{-2}$ towards W49N and G10.6–0.4, respectively.

The resulting NH mean abundances of all three methods in all velocity components are 5.5×10^{-9} and 1.1×10^{-8} in W49N and G10.6–0.4, respectively. This can be compared to the average $N(\text{NH})/N(\text{H}_2)$ value of 3×10^{-9} in diffuse and translucent sight-lines found by Weselak et al. (2009). The mean values of $o\text{-NH}_2$ are 3.1×10^{-9} and 4.5×10^{-9} in W49N and G10.6–0.4, respectively, and 1.5×10^{-9} and 1.9×10^{-9} for $o\text{-NH}_3$.

Our upper limits on the NH^+ abundances, relative to molecular hydrogen, are similar in both sources with mean value $N(\text{NH}^+)/N(\text{H}_2) \lesssim 4 \times 10^{-10}$. This is orders of magnitudes lower than previous findings from ultraviolet observations towards $\rho \text{ Oph}$ (Snow 1979; de Almeida & Singh 1982), but still much higher than the predictions from the chemical models presented in Paper I: approximately $10^{-13} - 10^{-14}$. The upper limits of the NH^+ abundance compared to NH are $\lesssim 2 - 14\%$ in the different velocity components (except in the uncertain velocity feature around $+33 \text{ km s}^{-1}$ in W49N), with a mean ratio of $\lesssim 6\%$. This is in contrast to the behaviour of CH^+ and marginally with that of OH^+ (Wyrowski et al. 2010; Gerin et al. 2010a) with respect to the corresponding neutrals. The CH^+ radical reaches comparable column densities to those of CH (e.g. Crane et al.

1995), and $N(\text{OH}^+)$ is a factor 30 below $N(\text{OH})$ in the visible data (Krelowski et al. 2010).

Since our different approaches to deconvolve the velocity components for the observed species agree well, we estimate that the uncertainties in our derived absolute column densities are $\lesssim 20 - 50\%$. The column densities for CH have larger uncertainties, but we estimate that the absolute $N(\text{CH})$ results are correct within a factor of approximately two. Furthermore, the scatter in the CH to H_2 relationship is estimated by Sheffer et al. (2008) to a factor of 1.6. In summary, we believe that the abundance determinations from CH are correct within a factor of a few. The abundance ratios of the nitrogen hydrides, relative to each other, are on the other hand more accurately determined.

The results of all three methods confirm our conclusion of the analysis of G10.6–0.4 in paper I that NH is more abundant than NH_2 and NH_3 by a factor of approximately 1.5–3.5, assuming the high temperature ortho-to-para limits of three and one, respectively. Note that the mean abundances of $o\text{-NH}_3$ are similar towards both sources, $\sim 2 \times 10^{-9}$, in contrast to $o\text{-NH}_2$, and, in particular NH, which have higher mean abundances towards G10.6–0.4 than towards W49N.

5.6. Comparison and correlations of species

Figures 8 and 9 show $o\text{-NH}_3$ and five SSB normalised comparison spectra, and in the on-line material Figs. G.9–G.10 we show additional comparisons of the nitrogen hydrides with the deconvolved CH absorption, the HI 21 cm line, H_2O^+ , OH^+ , HNC, CN, ortho- and para- H_2O , HF, and HCO^+ .

The CH spectra show absorption over a much wider range of velocities in both sources than the nitrogen hydrides. Ammonia largely follows the CH absorptions, but there are also large differences in some parts of the spectra where there is no or very little absorption of NH_3 , while CH shows a much broader and stronger absorption, for instance at $35 - 38$, $41 - 55$ and $65 - 70 \text{ km s}^{-1}$ towards W49N. Ammonia seems to trace CH slightly better towards G10.6–0.4 than W49N. This comparison suggests that CH exists in both relatively low and high density gas, while the nitrogen hydrides only exist in the parts of the interstellar gas with a relatively high density.

These differences are even more pronounced when comparing with neutral hydrogen as observed by the VLA $\lambda 21 \text{ cm}$ absorption by Fish et al. (2003), which shows absorption over a very wide range of velocities with a resolution of 2.5 km s^{-1} . The much more extended velocity space coverage of the HI absorption is expected since not all foreground clouds have molecular gas.

The ammonia absorption also follow similar trends as HCO^+ $J=1 \leftarrow 0$ (Godard et al. 2010), and H_2O , which is known to trace clouds of high molecular fraction (Neufeld et al. 2010b; Sonnentrucker et al. 2010). HCO^+ and H_2O seem to have a rather constant abundance ratio in these sight-lines, in contrast to their abundances with respect to ammonia. The comparison of ammonia to H_2O^+ and OH^+ , which mostly reside in lower density gas containing considerable amounts of atomic hydrogen (Gerin et al. 2010a; Neufeld et al. 2010a), shows no similarities.

When we compare ammonia with CN and HNC we find very similar absorption patterns. The CN $J=1 \leftarrow 0$ $F=1/2 - 3/2$, $1/2 - 1/2$ single hyperfine component and the HNC $J=1 \leftarrow 0$ line were observed with the IRAM 30 m antenna (Godard et al. 2010). Note, that HNC has three hfs components that, however, lie very close in velocities (0.2 and 0.5 km s^{-1}), which mostly leads to a broadening of the absorption features. These species mainly reside in denser gas than CH, and both

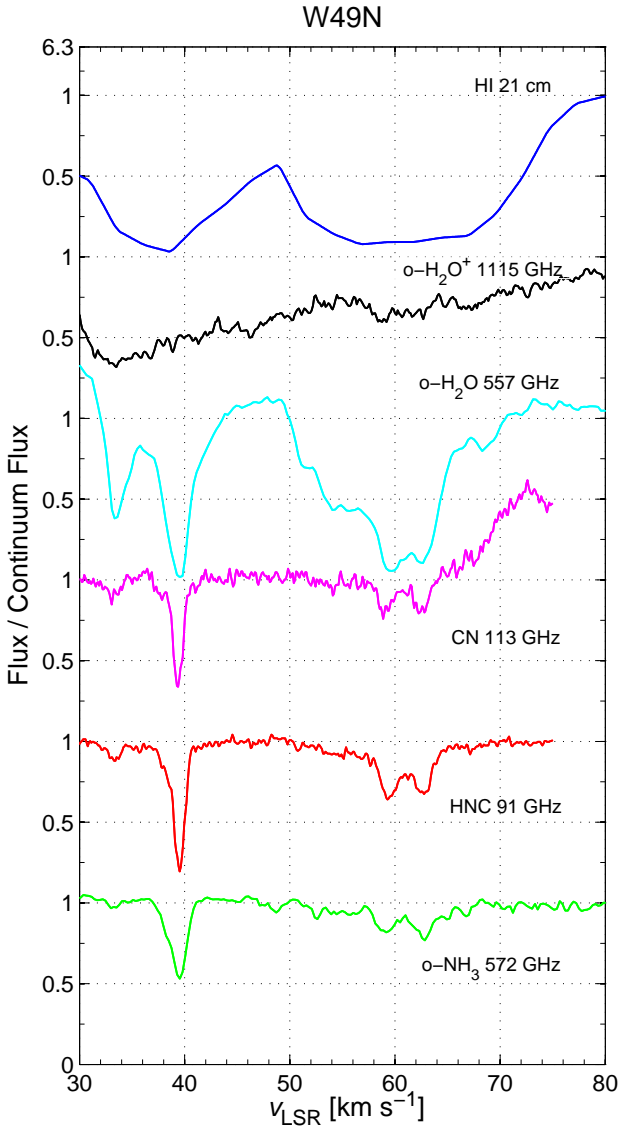


Fig. 8: *Line-of-sight absorptions towards W49N*: Normalised (SSB) spectra of ortho-ammonia and species tracing both high and low molecular fractions. Strong similarities are seen between ammonia, CN, HNC and water, but not with H_2O^+ and HI tracing the atomic diffuse gas.

are closely connected to the NH and NH_2 chemistry (e.g. Nejad et al. 1990; Liszt & Lucas 2001).

5.6.1. Column density correlations

In order to quantitatively examine abundance correlations of the nitrogen hydrides, CH, HNC and CN, we show column density plots in Figs. 10–11. We have here plotted the results from Method I. The parameters of the linear least square fits to the data are found in the figures in addition to the correlation coefficient R . In the on-line material we also show column density plots with all three methods (Figs. H.1–H.4).

Column density plots of the nitrogen hydrides are shown on the left hand side in Fig. 10. We note that the scatter is larger for $N(\text{NH})$ vs. $N(\text{o-NH}_3)$ than compared to $N(\text{o-NH}_2)$ vs. $N(\text{o-NH}_3)$ which show a rather tight correlation. This may indicate that NH does not entirely exist in the same gas as o-NH₂

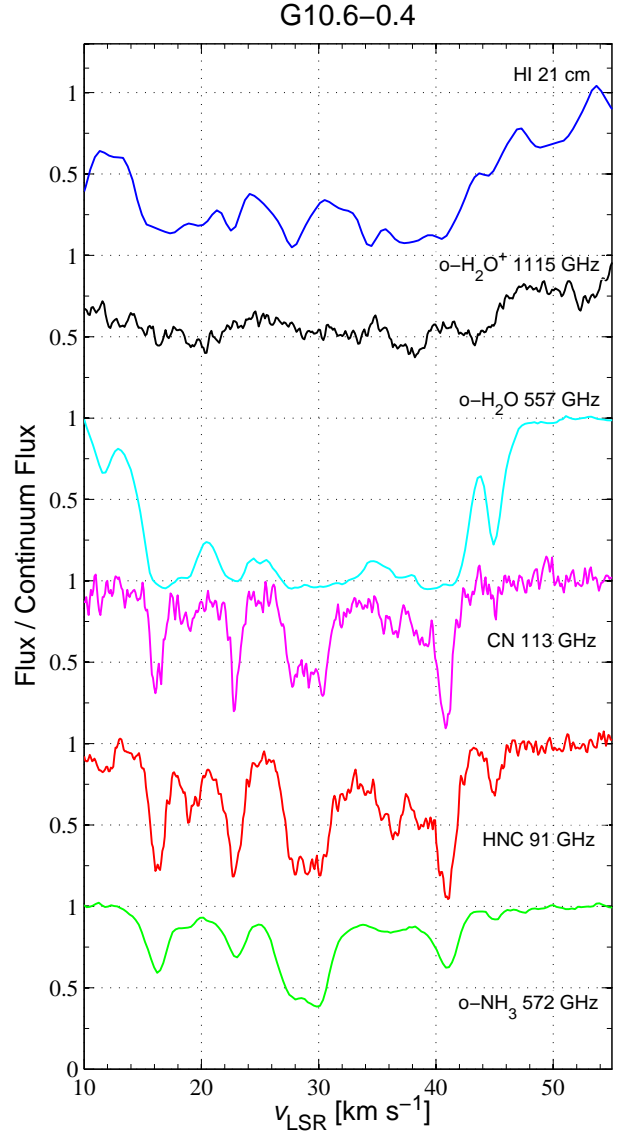


Fig. 9: *Line-of-sight absorptions towards G10.6–0.4*: Notation as in Fig. 8.

and o-NH₃. There is also a possibility that the NH and o-NH₃ correlation may only be valid for $N(\text{o-NH}_3) \lesssim 5 \times 10^{12} \text{ cm}^{-2}$. The $N(\text{NH})$ towards G10.6–0.4 appear to increase up to a maximum of $\sim 3 \times 10^{13} \text{ cm}^{-2}$. Also $N(\text{o-NH}_2)$ show a slight tendency of this behaviour towards G10.6–0.4 with a maximum of $\sim 1.2 \times 10^{13} \text{ cm}^{-2}$. This possible “chemical saturation” corresponds to a few A_V (estimated from our CH measurements and $N_{\text{H}} \sim 1.7 \times 10^{21} \text{ cm}^{-2} \text{ mag}^{-1} \times A_V$). This may be explained by a more efficient ammonia production at higher column densities, or that NH, and o-NH₂, are somehow consumed in the ammonia formation.

On the right hand side in Fig. 10 we show column density plots of the nitrogen hydrides vs. CH. The spread of the data points reflects the difficulty of finding a velocity structure common to hydrides and CH.

In Fig. 11 we show column density plots of the nitrogen hydrides vs. CN on the left and vs. HNC on the right. All three nitrogen hydrides show linear correlations with both CN and HNC. In dark cloud chemistry, CN and HNC are closely related

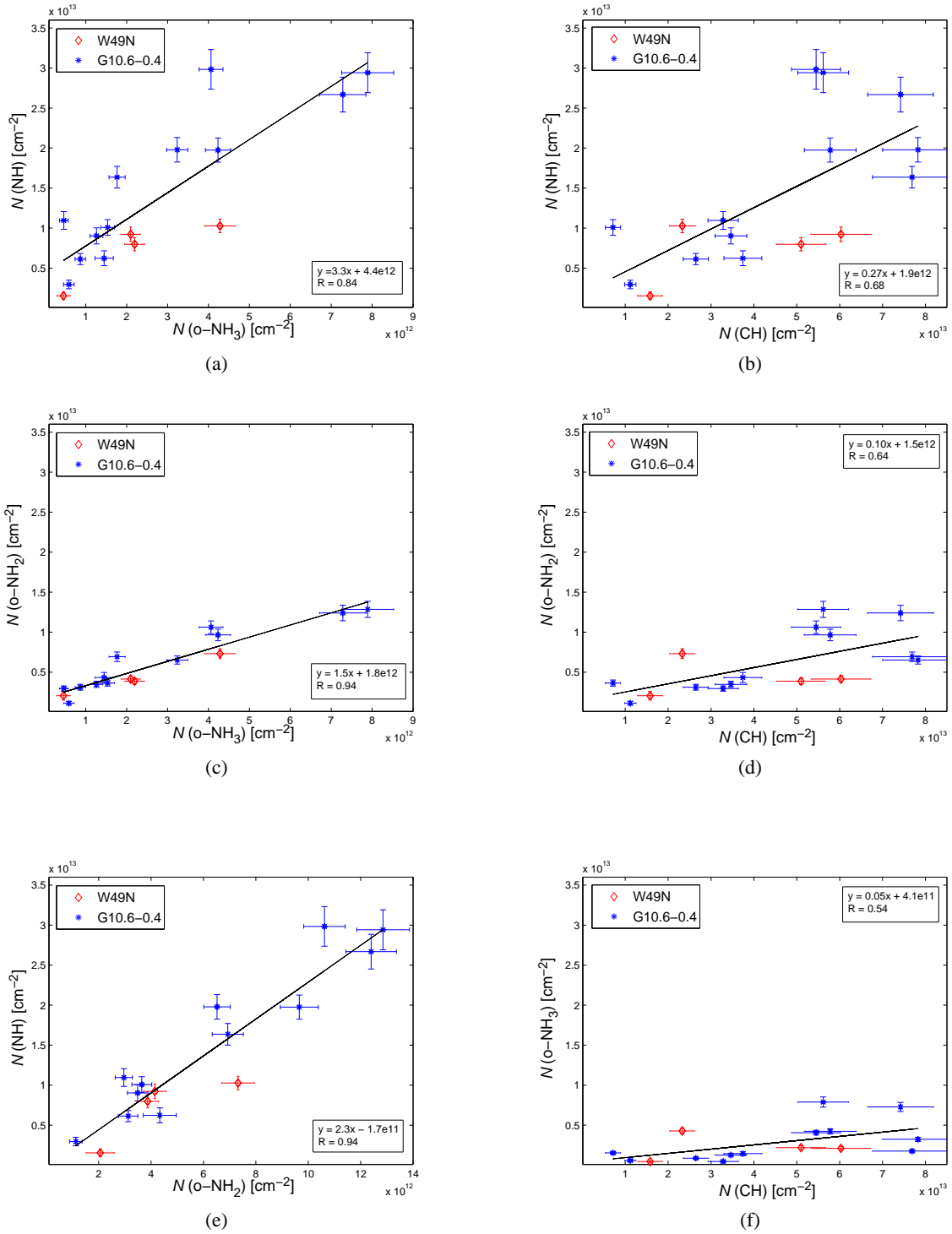


Fig. 10: Column density comparison plots. On the left hand side: NH, o-NH₂ and o-NH₃. On the right hand side: nitrogen hydrides vs. CH. The blue lines show linear least square fits to all data points towards both sources. The correlation coefficients and the linear fit equations are given in respective figure.

to NH and NH₂ through the reactions of $\text{C} + \text{NH}_2 \rightarrow \text{HNC} + \text{H}$, $\text{N} + \text{CH} \rightarrow \text{CN} + \text{H}$, and $\text{C} + \text{NH} \rightarrow \text{CN} + \text{H}$ (Nejad et al. 1990). Also Weselak et al. (2009) found a slightly better correlation between NH and CN than compared to CH, and no correlations with species such as CH⁺.

6. Ortho-to-para ratio of NH₃

There are two ways to produce molecules in interstellar space: in the gas-phase or on grain surfaces. If ammonia is formed in the gas-phase, by highly exoergic processes, the ammonia ortho-to-para ratio has been expected to be very close to the statistical

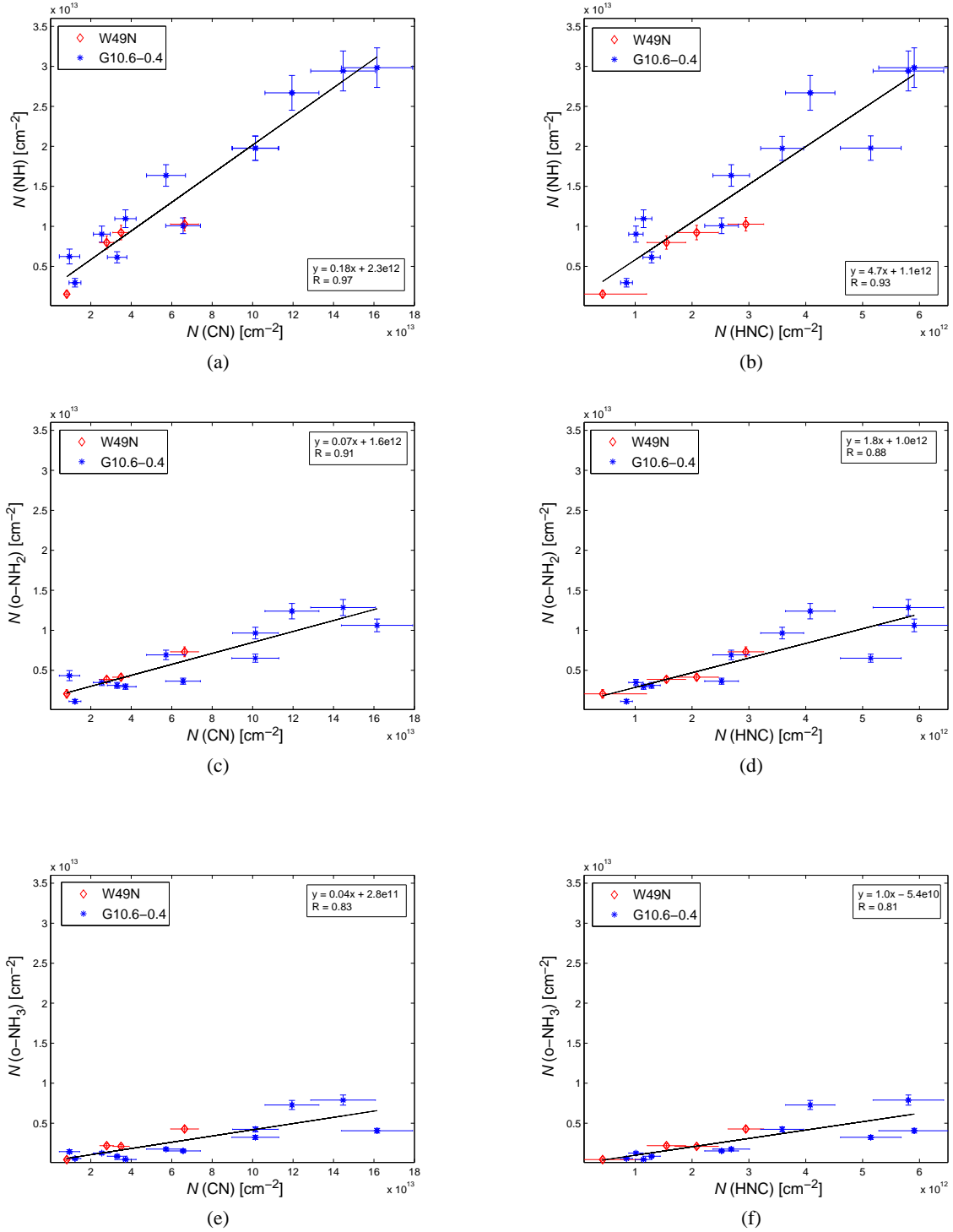


Fig. 11: Column density comparison plots. On the left hand side we show comparisons of the nitrogen hydrides with CN, and on the right hand side comparisons with HNC. Notation as in Fig. 10.

equilibrium value of 1.0 (the spin statistical value is 4–2 for ortho-para, but the number of para states is on the other hand almost a factor of two larger). If ammonia is formed at temperatures lower than 40 K on cold dust grains, and then desorbed when the grains are heated above 100 K, the OPR may differ from unity since the lowest ortho level is 22 K below the lowest para level. If no conversion processes between the two symme-

tries exist, the OPR of ammonia is expected to increase above unity at low formation temperatures.

Prior to Herschel, ortho-to-para ratios have been derived from measurements of inversion transitions, the (1, 1) and (2, 2) transitions involving para states, and the (3, 3) and (6, 6) transitions probing highly excited, metastable ortho states. For example, Umemoto et al. (1999) have found $\text{OPR} = 1.3 - 1.7$ in

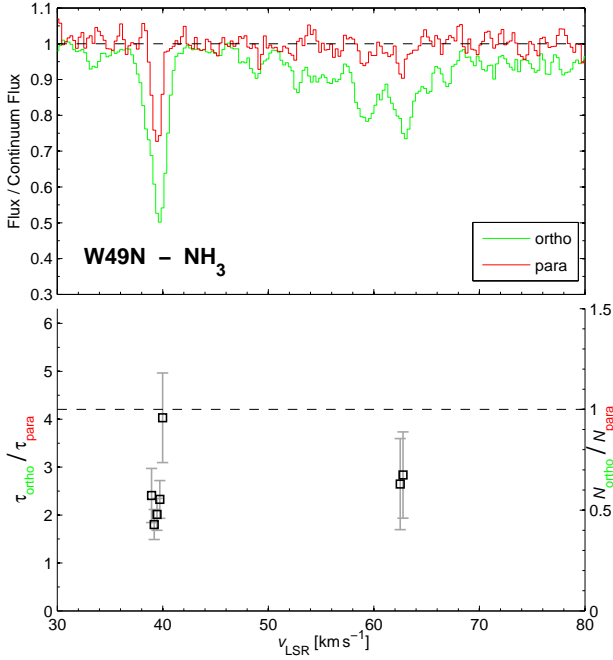


Fig. 12: W49N. (*Upper*) WBS spectra of 1_0-0_0 ortho-NH₃ and 2_1-1_1 para-NH₃ normalised to SSB continuum. (*Lower*) The optical depth ratios are shown for absorptions larger than 3σ as a function of LSR velocity. The column density ratios (OPR), estimated with RADEX, are given by the right hand y-axis. The horizontal dashed line marks an ortho-to-para optical depth ratio of 4.2 corresponding to a column density ratio of unity.

the L 1157 outflow from the observation of six inversion lines (J, K) = (1, 1) to (6, 6). Similarly, Nagayama et al. (2009) have inferred an even higher value of OPR = 1.5–3.5 in the central molecular zone of the Galaxy.

Using *Herschel*-HIFI observations of the fundamental rotational transitions of both ortho- and para-ammonia, it is for the first time possible to estimate the ammonia OPR in cold and diffuse interstellar gas of low excitation. Our results do, however, point to the surprising result of an OPR lower than unity.

This is shown in Figs. 12 and 13 where the upper panels show the normalised 1_0-0_0 ortho-NH₃ and 2_1-1_1 para-NH₃ spectra, and the lower panels show the corresponding optical depth ratios for absorptions larger than 3σ as a function of LSR velocity towards both sources (channel widths are 0.26 km s^{-1}). An ortho-to-para optical depth ratio of 4.2 corresponds to a column density ratio of unity using the RADEX conversion factors in Table 2. The resulting column density ratios are given by the right hand y-axis in both figures. The para line has lower S/N than the ortho line in both sources and several velocity components are weak. Still, most column density ratios are found to be below unity within the uncertainties.

We have also used Method I and II to estimate the OPR. Method I gives OPR(NH₃) = 0.7 ± 0.1 and $0.6-0.7 \pm 0.1$ in the strongest velocity components towards W49N ($+39 \text{ km s}^{-1}$ component) and G10.6–0.4 ($+16, 28, 30$ and 41 km s^{-1} components), respectively. The results from Method II gives similar results towards G10.6–0.4: $0.5-0.7 \pm 0.1$ in the velocity bins $v_{\text{LSR}} = 12.5-20, 25-29, 29-31$ and $39.5-43.5 \text{ km s}^{-1}$; but lower results towards W49N in $v_{\text{LSR}} = 36-42 \text{ km s}^{-1}, 0.4 \pm 0.2$.

The errors are dominated by the noise and the uncertainty in the sideband gain ratio. We have used the errors in sideband

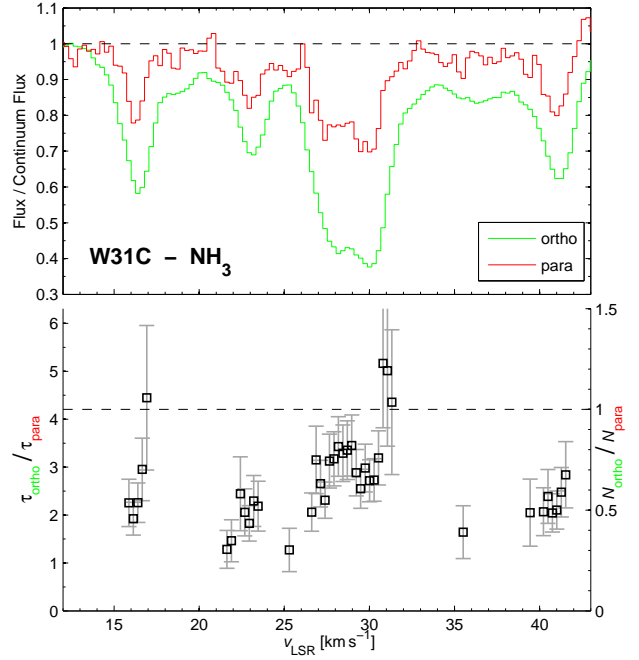


Fig. 13: G10.6–0.4 (W31C). Notation as in Fig. 12.

gain ratios stated on the *Herschel* internet site (4% for ortho and 6% for para). There is also an additional error arising from the rather large sideband separation of 12 GHz which means that the assumption of equal continuum temperature is not fully valid. This effect mimics a sideband gain ratio different from unity and is also taken into account (4 and 2% for ortho and para, respectively, estimated by $T_{\text{C,L}}/T_{\text{C,U}} = (v_{\text{L}}/v_{\text{U}})^{\beta}$ with $\beta = 2$). The errors from the noise is estimated by $\delta\tau = \exp(\tau) \times \delta I/I_0$, and the errors from the sideband gain ratio and differences in the continuum in the sidebands are estimated by $\delta\tau = \epsilon - \ln(1 + \epsilon \exp(\tau))$ where ϵ is both errors added in quadrature. The derivation of this formula assumes that the depth of the absorption line is correct, which means that $T_{\text{C}}(\text{SSB}) - T_{\text{A}}$ is conserved but the continuum level is not. The noise and calibration errors are finally added in quadrature. The error estimates for Method I and II add respective uncertainties from the methods to the calibration errors.

Some previous measurements of ammonia have resulted in an OPR lower than unity, although not in diffuse gas. In Orion KL Hermsen et al. (1988) obtained OPR(NH₃) = 0.5 from inversion emission lines, and Hermsen et al. (1985) found OPR(¹⁵NH₃) = 0.7. The latter low value was suggested to be caused by an excitation effect: a possible over-abundance of the unobserved $K = 0$ state. This explanation cannot be applied in our case, since we actually observe the $K = 0$ ortho state. Flower et al. (1995) modelled several NH₃ inversion transitions in the frame of C-shock models towards the warm and dense Sgr B2 envelope and their best OPR of ammonia was ~ 0.5 , also lower than the statistical value of unity. Ceccarelli et al. (2002), however, observed 21 high excitation ortho- and para-ammonia lines, both metastable and non-metastable levels, towards Sgr B2 using ISO, and derived an ammonia OPR of unity.

There are to our knowledge no previous estimate of the OPR(NH₃) in *diffuse* gas, and it may very well be very different from the OPR in dense gas. We can, however, compare our strong absorption of the para-NH₃ line to the observations by Tieftrunk et al. (1994) who observed the two lowest inversion lines of para-NH₃ towards W49N. Their estimate of $N(\text{p-NH}_3)$ is

$2.5 \times 10^{12} \text{ cm}^{-2}$ which is less than half our value, $\sim 6 \times 10^{12} \text{ cm}^{-2}$. If this column density is correct, it would imply an OPR higher than unity in this velocity component in W49N. In our excitation model, however, the integrated optical depth observed by Tieftrunk et al. (1994) in the 1_1 inversion line at $+39 \text{ km s}^{-1}$ implies a $N(\text{p-NH}_3)$ in good agreement with our value, since we obtain a higher excitation temperature than the 2.7 K used by Tieftrunk et al. (1994) for the 1_1 inversion transition.

We have no clear explanation yet of our surprising result and we can only speculate about its origin. Either there are to us unknown instrumental effects, or that our assumption that the line-of-sight gas completely covers the background continuum within the beam is not correct, or there must exist some physical or chemical processes that affect the OPR in diffuse gas. In general, the fact that interstellar clouds are weak plasmas allows for conversion processes at low temperatures that would not be present in a purely neutral gas. What OPR these processes lead to must be determined by careful modelling. In diffuse molecular clouds of relatively low density, $n(\text{H}_2) \lesssim 10^3$, but relatively high ionisation fraction, $n(e)/n(\text{H}_2) \gtrsim 10^{-4}$, the rate of destruction of NH_3 by reactions with C^+ , H^+ , and H_3^+ , can be as high as 10^{-9} s^{-1} at kinetic temperatures $T \sim 30 \text{ K}$. The latter two ions can also interchange ortho and para states directly by proton substitution, perhaps at a comparable rate. These rates of destruction and interchange can approach the rates of radiative and collisional excitation out of the metastable levels, which means that the excitation and chemistry of NH_3 should be treated together in a self-consistent fashion. Under these conditions, NH_3 is a non-equilibrium system and a “spin temperature” derived from an ortho-to-para ratio is not expected to be meaningful.

The NH_4^+ molecule could also affect the ammonia OPR in a similar manner. The fastest gas-phase reaction sequence of ammonia is



where N^+ is formed by cosmic ray ionisation, or by reactions of He^+ with N_2 or CN which are formed by neutral-neutral reactions. Whether or not ammonia is produced on grains or in the gas, its destruction in the gas by protonating ions such as H_3^+ also leads to NH_4^+ , which can have a variety of nuclear spin states depending on the overall nuclear spin of H_3^+ . The ammonia OPR could then simply reflect the spin states of NH_4^+ .

In addition, some laboratory evidence exists that dissociative recombination reactions have different rate coefficients depending upon the nuclear spin configuration of the molecular ion.

Observations of the ortho-to-para ratio of NH_3 could thus provide a valuable insight into the competing processes of formation and destruction, radiative and collisional excitation, and reactive interchange processes.

7. Summary

Our spectrally resolved rotational transitions of NH , o-NH_2 , ortho- and para- NH_3 along the sight-lines towards the high-mass star-forming regions W49N and G10.6–0.4 show remarkable similarities of line profiles and abundances. We find similar abundances of all three species and a co-existence in diffuse or translucent interstellar gas with a high molecular fraction. The mean abundance of ortho- NH_3 abundance is $\sim 2 \times 10^{-9}$ towards both sources. The mean ratios of all three methods of the nitrogen hydrides in all velocity components, are $N(\text{NH})/N(\text{o-NH}_3) = 5.9$ and 3.5 , and $N(\text{o-NH}_2)/N(\text{o-NH}_3) = 2.4$ and 2.0 , towards G10.6–0.4 and W49N, respectively. This is in

sharp contrast to previous observations of the nitrogen hydrides in dark clouds where the ammonia abundances are found to be ~ 100 times higher than $X(\text{NH})$, and ~ 10 – 300 times higher than $X(\text{NH}_2)$. NH and o-NH_2 are found to be linearly correlated with o-NH_3 at least for $N(\text{o-NH}_3) \lesssim 5 \times 10^{12} \text{ cm}^{-2}$ which corresponds to a few A_V . Upper limits of $N(\text{NH}^+)$ in both sources indicate a $N(\text{NH}^+)/N(\text{NH})$ ratio of $\lesssim 2$ – 14% , with a mean of $\lesssim 6\%$.

Linear correlations are also found for all three nitrogen hydrides with respect to CH , CN and HNC , although CH displays a more loose correlation than the latter two species. The nitrogen hydrides also largely follow the absorption pattern in Doppler velocity space of HCO^+ and water, a species also known to trace regions of a high molecular fraction.

We have obtained a surprisingly low ortho-to-para ratio of ammonia, ≈ 0.5 – 0.7 ± 0.1 , in the strongest velocity components, which is below the high-temperature limit of unity. No clear explanation has been found. More observations are needed of both the rotational transitions and the inversion lines with ground-based facilities, to be able to make firm conclusions about the ammonia OPR in diffuse gas.

We will continue to investigate the absorption lines in the sight-lines towards the other six PRISMAS sources. This will allow an analysis of the nitrogen chemistry at various galactic distances from the Galactic Centre. We will also use new Open Time 1 (OT1) *Herschel*-HIFI data of higher excitation lines to analyse the hot core sources which will be compared and contrasted with the diffuse interstellar gas. The ortho-to-para ratio of NH_3 will also be further investigated both in the sources and in the diffuse gas, in addition to the OPR of NH_2 , for which new OT1 data in four of the PRISMAS sources will be analysed and compared to the ammonia OPR.

Acknowledgements. The *Herschel* spacecraft was designed, built, tested, and launched under a contract to ESA managed by the *Herschel*/Planck Project team by an industrial consortium under the overall responsibility of the prime contractor Thales Alenia Space (Cannes), and including Astrium (Friedrichshafen) responsible for the payload module and for system testing at spacecraft level, Thales Alenia Space (Turin) responsible for the service module, and Astrium (Toulouse) responsible for the telescope, with in excess of a hundred subcontractors. HIFI has been designed and built by a consortium of institutes and university departments from across Europe, Canada and the United States under the leadership of SRON Netherlands Institute for Space Research, Groningen, The Netherlands and with major contributions from Germany, France and the US. Consortium members are: Canada: CSA, U.Waterloo; France: CESR, LAB, LERMA, IRAM; Germany: KOSMA, MPIFR, MPS; Ireland, NUI Maynooth; Italy: ASI, IFSI-INAF, Osservatorio Astrofisico di Arcetri- INAF; Netherlands: SRON, TUD; Poland: CAMK, CBK; Spain: Observatorio Astronómico Nacional (IGN), Centro de Astrobiología (CSIC-INTA). Sweden: Chalmers University of Technology - MC2, RSS & GARD; Onsala Space Observatory; Swedish National Space Board, Stockholm University - Stockholm Observatory; Switzerland: ETH Zurich, FHNW; USA: Caltech, JPL, NHSC. CP and JHB acknowledge generous support from the Swedish National Space Board. MdL and MG acknowledge funding by CNES and by the ANR SCHISM project (ANR-09-BLAN-0231-01). T.A.B., B.G. and J.R.G. thank the Spanish MICINN for funding support through grants AYA2009-07304 and CSD2009-00038. H.S.P.M. is very grateful to the Bundesministerium für Bildung und Forschung (BMBF) for financial support aimed at maintaining the Cologne Database for Molecular Spectroscopy, CDMS. This support has been administered by the Deutsches Zentrum für Luft- und Raumfahrt (DLR). We also thank the referee Harvey Liszt whose constructive comments led to a significant improvement of the paper.

References

- Adande, G. & Ziurys, L. 2011, in IAU Symposium, Vol. 280, IAU Symposium, 76P
- Bacmann, A., Caux, E., Hily-Blant, P., et al. 2010, *A&A*, 521, L42
- Biver, N., Bockelée-Morvan, D., Crovisier, J., et al. 2007, *Planet. Space Sci.*, 55, 1058
- Cazzoli, G., Dore, L., & Puzzarini, C. 2009, *A&A*, 507, 1707

- Ceccarelli, C., Baluteau, J.-P., Walmsley, M., et al. 2002, *A&A*, 383, 603
 Cernicharo, J., Goicoechea, J. R., & Caux, E. 2000, *ApJ*, 534, L199
 Cheung, A. C., Rank, D. M., Townes, C. H., Thornton, D. D., & Welch, W. J. 1968, *Physical Review Letters*, 21, 1701
 Comito, C., Schilke, P., Phillips, T. G., et al. 2005, *ApJS*, 156, 127
 Coudert, L. H. & Roueff, E. 2006, *A&A*, 449, 855
 Coudert, L. H. & Roueff, E. 2009, *A&A*, 499, 347
 Crane, P., Lambert, D. L., & Sheffer, Y. 1995, *ApJS*, 99, 107
 Crawford, I. A. & Williams, D. A. 1997, *MNRAS*, 291, L53
 Dame, T. M. & Thaddeus, P. 1985, *ApJ*, 297, 751
 de Almeida, A. A. & Singh, P. D. 1982, *A&A*, 113, 199
 de Graauw, T., Helmich, F. P., Phillips, T. G., et al. 2010, *A&A*, 518, L4
 De Pree, C. G., Wilner, D. J., Goss, W. M., Welch, W. J., & McGrath, E. 2000, *ApJ*, 540, 308
 Dickel, H. R. & Goss, W. M. 1990, *ApJ*, 351, 189
 Dreher, J. W., Johnston, K. J., Welch, W. J., & Walker, R. C. 1984, *ApJ*, 283, 632
 Farmer, C. B. & Norton, R. H. 1989, A high-resolution atlas of the infrared spectrum of the sun and the earth atmosphere from space. A compilation of ATMOS spectra of the region from 650 to 4800 cm^{-1} (2.3 to 16 μm). Vol. I. The sun., ed. Farmer, C. B. & Norton, R. H.
 Feldman, P. D., Fournier, K. B., Grinin, V. P., & Zvereva, A. M. 1993, *ApJ*, 404, 348
 Fish, V. L., Reid, M. J., Wilner, D. J., & Churchwell, E. 2003, *ApJ*, 587, 701
 Flores-Mijangos, J., Brown, J. M., Matsushima, F., et al. 2004, *Journal of Molecular Spectroscopy*, 225, 189
 Flower, D. R., Pineau des Forets, G., & Walmsley, C. M. 1995, *A&A*, 294, 815
 Gerin, M., de Luca, M., Black, J., et al. 2010a, *A&A*, 518, L110
 Gerin, M., de Luca, M., Goicoechea, J. R., et al. 2010b, *A&A*, 521, L16
 Godard, B., Falgarone, E., Gerin, M., Hily-Blant, P., & de Luca, M. 2010, *A&A*, 520, A20+
 Goicoechea, J. R., Rodríguez-Fernández, N. J., & Cernicharo, J. 2004, *ApJ*, 600, 214
 Hasegawa, T. I. & Herbst, E. 1993, *MNRAS*, 263, 589
 Hasegawa, T. I., Kwok, S., Koning, N., et al. 2006, *ApJ*, 637, 791
 Hermsen, W., Wilson, T. L., Walmsley, C. M., & Batrla, W. 1985, *A&A*, 146, 134
 Hermsen, W., Wilson, T. L., Walmsley, C. M., & Henkel, C. 1988, *A&A*, 201, 285
 Hily-Blant, P., Maret, S., Bacmann, A., et al. 2010, *A&A*, 521, L52
 Ho, P. T. P. & Townes, C. H. 1983, *ARA&A*, 21, 239
 Hübers, H., Evenson, K. M., Hill, C., & Brown, J. M. 2009, *J. Chem. Phys.*, 131, 034311
 Keene, J., Blake, G. A., & Phillips, T. G. 1983, *ApJ*, 271, L27
 Klaus, T., Takano, S., & Winnewisser, G. 1997, *A&A*, 322, L1
 Knauth, D. C., Andersson, B., McCandliss, S. R., & Warren Moos, H. 2004, *Nature*, 429, 636
 Krelowski, J., Beletsky, Y., & Galazutdinov, G. A. 2010, *ApJ*, 719, L20
 Langer, W. D. & Graedel, T. E. 1989, *ApJS*, 69, 241
 Larsson, B., Liseau, R., Bergman, P., et al. 2003, *A&A*, 402, L69
 Lis, D. C., Wootten, A., Gerin, M., & Roueff, E. 2010, *ApJ*, 710, L49
 Liseau, R., Larsson, B., Brandeker, A., et al. 2003, *A&A*, 402, L73
 Liszt, H. & Lucas, R. 2001, *A&A*, 370, 576
 Liszt, H. S., Lucas, R., & Pety, J. 2006, *A&A*, 448, 253
 Markwardt, C. B. 2009, in *Astronomical Society of the Pacific Conference Series*, Vol. 411, *Astronomical Data Analysis Software and Systems XVIII*, ed. D. A. Bohlender, D. Durand, & P. Dowler, 251+
 Marshall, D. J., Robin, A. C., Reylé, C., Schultheis, M., & Picaud, S. 2006, *A&A*, 453, 635
 Marty, B., Chaussidon, M., Wiens, R. C., Jurewicz, A. J. G., & Burnett, D. S. 2011, *Science*, 332, 1533
 Meier, R., Wellnitz, D., Kim, S. J., & A'Hearn, M. F. 1998, *Icarus*, 136, 268
 Meyer, D. M. & Roth, K. C. 1991, *ApJ*, 376, L49
 Millar, T. J., Bennett, A., Rawlings, J. M. C., Brown, P. D., & Charnley, S. B. 1991, *A&AS*, 87, 585
 Müller, H. S. P., Klein, H., Belov, S. P., et al. 1999, *Journal of Molecular Spectroscopy*, 195, 177
 Müller, H. S. P., Schlöder, F., Stutzki, J., & Winnewisser, G. 2005, *Journal of Molecular Structure*, 742, 215
 Nagayama, T., Omodaka, T., Handa, T., et al. 2009, *PASJ*, 61, 1023
 Nash, A. G. 1990, *ApJS*, 72, 303
 Nejad, L. A. M., Williams, D. A., & Charnley, S. B. 1990, *MNRAS*, 246, 183
 Neufeld, D. A., Goicoechea, J. R., Sonnentrucker, P., et al. 2010a, *A&A*, 521, L10
 Neufeld, D. A., Sonnentrucker, P., Phillips, T. G., et al. 2010b, *A&A*, 518, L108
 Nyman, L.-A. & Millar, T. J. 1989, *A&A*, 222, 231
 Ott, S. 2010, in *Astronomical Society of the Pacific Conference Series*, Vol. 434, *Astronomical Data Analysis Software and Systems XIX*, ed. Y. Mizumoto, K.-I. Morita, & M. Ohishi, 139
 Persson, C. M., Black, J. H., Cernicharo, J., et al. 2010, *A&A*, 521, L45 (Paper I)
 Persson, C. M., Olberg, M., Hjalmarson, Å., et al. 2009, *A&A*, 494, 637
 Pickett, H. M., Poynter, I. R. L., Cohen, E. A., et al. 1998, *Journal of Quantitative Spectroscopy and Radiative Transfer*, 60, 883
 Pilbratt, G., Riedinger, J. R., Passvogel, T., et al. 2010, *A&A*, 518, L1
 Plume, R., Kaufman, M. J., Neufeld, D. A., et al. 2004, *ApJ*, 605, 247
 Polehampton, E. T., Baluteau, J., Swinyard, B. M., et al. 2007, *MNRAS*, 377, 1122
 Rist, C., Alexander, M. H., & Valiron, P. 1993, *J. Chem. Phys.*, 98, 4662
 Roelfsema, P. R., Helmich, F. P., Teyssier, D., et al. 2012, *A&A*, 537, A17
 Sandford, S. A., Bernstein, M. P., Allamandola, L. J., Goorvitch, D., & Teixeira, T. C. V. S. 2001, *ApJ*, 548, 836
 Schmitt, J. L. 1969, *PASP*, 81, 657
 Sheffer, Y., Rogers, M., Federman, S. R., et al. 2008, *ApJ*, 687, 1075
 Snow, T. P. & McCall, B. J. 2006, *ARA&A*, 44, 367
 Snow, Jr., T. P. 1979, *Ap&SS*, 66, 453
 Sonnentrucker, P., Neufeld, D. A., Phillips, T. G., et al. 2010, *A&A*, 521, L12
 Swings, P., Elvey, C. T., & Babcock, H. W. 1941, *ApJ*, 94, 320
 Tieftrunk, A., Pineau des Forets, G., Schilke, P., & Walmsley, C. M. 1994, *A&A*, 289, 579
 Umemoto, T., Mikami, H., Yamamoto, S., & Hirano, N. 1999, *ApJ*, 525, L105
 van der Tak, F. F. S., Black, J. H., Schöier, F. L., Jansen, D. J., & van Dishoeck, E. F. 2007, *A&A*, 468, 627
 van Dishoeck, E. F., Jansen, D. J., Schilke, P., & Phillips, T. G. 1993, *ApJ*, 416, L83
 Varberg, T. D., Stroh, F., & Evenson, K. M. 1999, *Journal of Molecular Spectroscopy*, 196, 5
 Verhoeve, P., Ter Meulen, J. J., Meerts, W. L., & Dyamanus, A. 1986, *Chemical Physics Letters*, 132, 213
 Wagenblast, R., Williams, D. A., Millar, T. J., & Nejad, L. A. M. 1993, *MNRAS*, 260, 420
 Weselak, T., Galazutdinov, G. A., Beletsky, Y., & Krelowski, J. 2009, *MNRAS*, 400, 392
 Wilson, T. L. & Rood, R. 1994, *ARA&A*, 32, 191
 Wirstrom, E. S., Bergman, P., Black, J. H., et al. 2010, *A&A*, 522, A19
 Wyrowski, F., Menten, K. M., Güsten, R., & Belloche, A. 2010, *A&A*, 518, A26

Appendix A: Herschel observations

Table A.1: *Herschel* OBSID's of the observed transitions analysed in this paper.

Source	Species	Frequency (GHz)	Band	LO-setting ^a	Date	OBSID
W49N	NH ^b	946.476	3b	A	2010-04-13	1342194700
				B		1342194701
				C		1342194702
	NH	974.478	4a	A	2010-04-18	1342195004
				B		1342195005
				C		1342195006
	o-NH ₂	952.578	3b	A	2010-04-13	1342194706
				B		1342194707
				C		1342194708
	o-NH ₃	572.498	1b	A	2010-04-11	1342194517
				B		1342194518
				C		1342194519
	p-NH ₃ ^c	1215.246	5a	A	2010-04-18	1342195067
				B		1342195068
				C		1342195069
NH ⁺	1012.540	4a	A	2010-04-18	1342194998	
			B		1342194999	
			C		1342195000	
G10.6-0.4	NH ^b	946.476	3b	A	2010-03-18	1342192316
				B		1342192317
				C		1342192318
	NH	974.478	4a	A	2010-03-03	1342191620
				B		1342191621
				C		1342191622
	o-NH ₂	952.578	3b	A	2010-03-18	1342192319
				B		1342192320
				C		1342192321
	o-NH ₃	572.498	1b	A	2010-03-02	1342191578
				B		1342191579
				C		1342191580
	p-NH ₃ ^c	1215.246	5a	A	2010-03-05	1342191697
				B		1342191698
				C		1342191699
NH ⁺	1012.540	4a	A	2010-03-03	1342191623	
			B		1342191624	
			C		1342191625	

Notes. ^(a) Three different frequency settings of the LO were performed, with approximately 15 km s⁻¹ between each setting in order to determine the sideband origin of the signals. ^(b) Observed in the same setting as CH₂ at 946 GHz. ^(c) The ortho-NH₃ 2₀ – 1₀ transition at 1214.859 GHz is observed in the same setting as para-NH₃ 2₁ – 1₁ at 1215.246 GHz

Appendix B: Emission line contamination of o-NH₂ towards W49N

identified as the hfs blend in the lower half of the same spin-rotation doublet of NO $^2\Pi_{1/2}$ $J = 9.5^e \rightarrow 8.5^e$ at an average rest frequency of 952.145441 GHz. The PRISMAS observations have also found three additional NO lines in W49N shown in Fig. B.2, each one consisting of unresolved hfs components, while no emission of NO is found in G10.6–0.4.

Since the two NO lines seen in Fig. B.3 have almost equal line strength, and are also observed with the same instrument in the same band, we have used the observed 952.145 GHz transition as a template to remove the interfering NO line at 952.464 GHz from the o-NH₂ absorption. In order to do this we use

$$T_{\text{norm}} = \frac{T_A - T_C}{T_C + T_{\text{NO}}}, \quad (\text{B.1})$$

to calculate the normalised SSB intensity T_{norm} in K, where T_C is the SSB continuum, and T_{NO} is the intensity of the NO line ($T_A - T_{C,\text{DSB}}$). The model NO line, shown in Fig. B.1, is then moved to the velocity of the emission line. The resulting absorption line spectrum of o-NH₂ towards W49N with removed NO emission is shown in green in Fig. B.3.

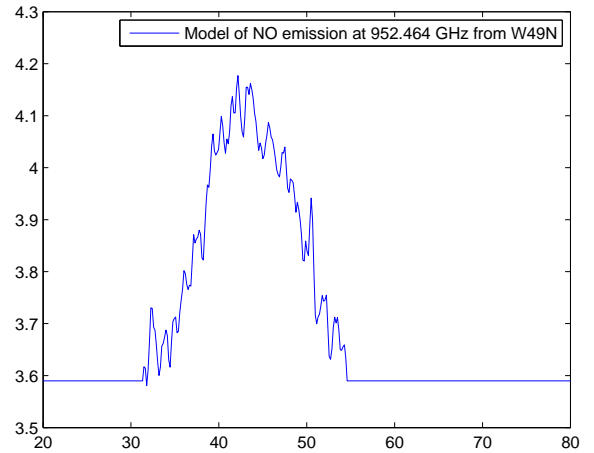


Fig. B.1: W49N: Model of the 952.464 GHz NO line to be removed from the o-NH₂ absorption lines. The model is using the NO 952.145 GHz emission line observed at $v_{\text{LSR}} = +7.7 \text{ km s}^{-1}$ and only shifted in velocity to a v_{LSR} of $+43.5 \text{ km s}^{-1}$ corresponding to a v_{LSR} of $+7.7 \text{ km s}^{-1}$ for that line.

The o-NH₂ absorption towards W49N is contaminated by an emission line in the same sideband from the source, a more complicated situation than an emission line from the other sideband. In Fig. B.3 an emission line is clearly visible around 47 km s^{-1} in the o-NH₂ spectrum. Here, the intensities have been normalised to the continuum in single sideband as $T_A/T_C - 1$ assuming a sideband gain ratio of unity where T_A is the observed intensity and T_C is the SSB continuum as measured in line-free regions in the spectra. We identify the emission line as a blend of three unresolved hfs components of NO $^2\Pi_{1/2}$ $J = 9.5^f \rightarrow 8.5^f$, $F = 10.5 - 9.5$, $9.5 - 8.5$, and $8.5 - 9.5$, at 952.464201 GHz (weighted mean frequency, cf. Varberg et al. 1999). The emission line appearing near 142 km s^{-1} in this figure is consequently

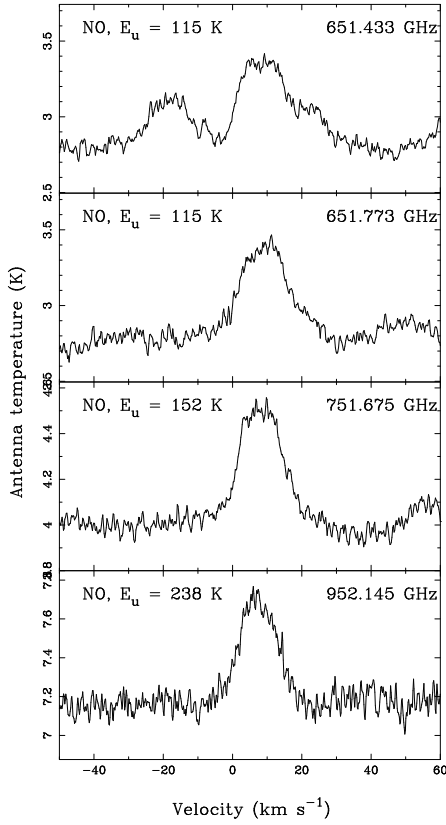


Fig. B.2: *W49N*: Double sideband WBS spectra of four NO emission lines from the source itself. Each NO line consists of 3 hfs components, with quantum numbers ${}^2\Pi_{1/2} J = 6.5^e \rightarrow 5.5^e$ (651 GHz), $J = 6.5^f \rightarrow 5.5^f$ (652 GHz), $J = 7.5^e \rightarrow 6.5^e$ (752 GHz), and $J = 9.5^e \rightarrow 8.5^e$ (952 GHz). The emission line at -18 km s^{-1} blended with NO 651.433 GHz is SO $11_{11} - 11_{10}$.

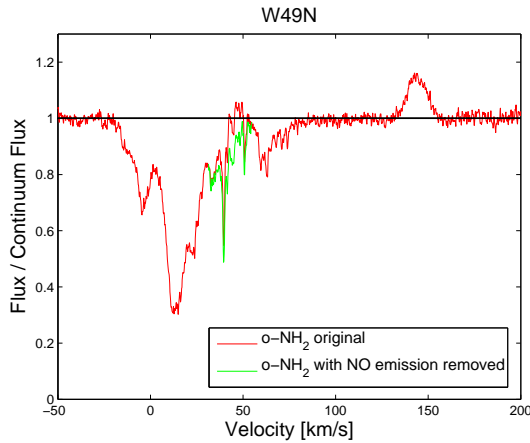


Fig. B.3: *NO* emission from *W49N* in the line-of-sight *o-NH*₂ absorption.: Normalised SSB spectrum of *o-NH*₂. The emission line at 142 km s^{-1} is from NO at $\nu_0 = 952.145 \text{ GHz}$. The NO $\nu_0 = 952.464 \text{ GHz}$ emission feature is seen at 47 km s^{-1} in the *o-NH*₂ absorption. The two NO lines have similar line strengths. The red line shows the SSB normalised *o-NH*₂ line without removal of the NO-line, and the green shows the spectra with removed NO-line.

Appendix C: Hyperfine structure componentsTable C.1: Hyperfine structure components of $\text{NH } ^3\Sigma^-$ $N=1 \leftarrow 0, J=2 \leftarrow 1$.

Frequency (MHz)	A_{ul} (s^{-1})	Δv^a (km s^{-1})	Rel. Intensity $\frac{A_{ul} \times g_u}{A_{ul}(\text{main}) \times g_u(\text{main})}^b$
974315.58	1.78e-6	50.08	0.0001
974342.57	6.02e-6	41.78	0.0007
974354.64	4.54e-6	38.07	0.0003
974410.56	8.91e-5	20.87	0.006
974411.39	5.13e-4	20.61	0.018
974436.35	2.28e-3	12.93	0.164
974437.54	1.27e-3	12.56	0.137
974444.04	1.81e-3	10.56	0.130
974450.44	4.80e-3	8.60	0.173
974462.22	5.04e-4	4.97	0.363
974471.00	5.67e-3	2.27	0.612
974475.41	3.38e-3	0.91	0.243
974478.38	6.94e-3	0	1.0
974479.34	6.01e-3	-0.30	0.649
974531.32	2.59e-4	-16.29	0.019
974539.82	6.46e-4	-18.90	0.023
974558.07	9.82e-4	-24.52	0.035
974564.78	7.67e-4	-26.58	0.055
974574.43	8.15e-4	-29.55	0.088
974583.03	2.59e-4	-32.20	0.019
974607.78	1.21e-4	-39.81	0.013

Notes. ^(a) The velocity offset from the strongest hfs component at 974478.38 MHz. ^(b) The sum of the relative intensities of the 21 hfs components is 3.75.

Table C.2: Hyperfine structure components of $\text{NH } ^3\Sigma^-$ $N=1 \leftarrow 0, J=0 \leftarrow 1$.

Frequency (MHz)	A_{ul} (s^{-1})	Δv^a (km s^{-1})	Rel. Intensity $\frac{A_{ul} \times g_u}{A_{ul}(\text{main}) \times g_u(\text{main})}^b$
946380.79	2.40e-3	30.100375183108216	0.369
946380.79	9.58e-4	30.100375183108216	0.295
946419.79	3.66e-4	17.746741564471662	0.056
946419.98	8.99e-4	17.688682017264846	0.276
946475.82	3.25e-3	0	1.0
946509.24	1.93e-3	-10.586919289910648	0.297
946509.24	1.21e-3	-10.586919289910648	0.372
946527.48	1.81e-3	-16.363416629849031	0.278
946527.56	1.84e-4	-16.389231431253044	0.057

Notes. ^(a) The velocity offset from the strongest hfs component at 946475.82 MHz. ^(b) The sum of the relative intensities of the 9 hfs components is 3.66.

Table C.3: Hyperfine structure components of ortho- NH_2 $1_{1,1} - 0_{0,0}$.

Frequency (MHz)	A_{ul} (s^{-1})	Δv^a (km s^{-1})	Rel. Intensity $\frac{A_{ul} \times g_u}{A_{ul}(\text{main}) \times g_u(\text{main})}^b$
952435.66	4.86e-6	44.91	0.0002
952446.99	1.33e-5	41.34	0.0006
952463.69	3.07e-5	36.09	0.002
952490.73	3.5e-3	27.58	0.079
952502.06	1.28e-3	24.01	0.029
952503.09	1.79e-3	23.69	0.081
952514.42	3.65e-3	20.12	0.164
952528.90	2.03e-3	15.56	0.046
952533.03	2.23e-4	14.27	0.010
952540.23	6.53e-3	12.00	0.147
952542.21	7.02e-3	11.37	0.474
952549.73	2.63e-3	9.01	0.178
952560.41	3.32e-3	5.65	0.149
952562.12	6.42e-3	5.11	0.289
952571.74	7.55e-3	2.08	0.340
952573.46	3.88e-3	1.54	0.174
952577.11	8.47e-3	0.39	0.570
952578.35	1.11e-2	0	1.0
952600.46	1.59e-3	-6.96	0.072
952615.49	3.58e-3	-11.69	0.081
952626.82	2.73e-3	-15.25	0.061
952627.84	2.67e-3	-15.57	0.120
952628.25	3.35e-3	-15.70	0.226
952639.17	1.40e-3	-19.14	0.063
952653.66	9.66e-3	-23.70	0.022
952655.64	7.43e-4	-24.32	0.050
952659.49	4.40e-4	-25.54	0.020
952664.99	1.58e-3	-27.27	0.036
952686.88	2.97e-4	-34.16	0.013
952698.21	7.06e-5	-37.72	0.003

Notes. ^(a) The velocity offset from the strongest hfs component at 952578.35 MHz. ^(b) The sum of the relative intensities of the 30 hfs components is 4.50.

Table C.4: Hyperfine structure components of ortho- NH_3 $1_0 - 0_0$.

Frequency ^a (MHz)	Δv^b (km s^{-1})	Rel. Intensity ^{a,c}
572.4971	-1.0473	0.1999
572.4984	0.0	1.0
572.5002	0.5237	0.6

Notes. ^(a) From Cazzoli et al. (2009). ^(b) The velocity offset from the strongest hfs component at 572.4984 MHz. ^(c) The sum of the relative intensities of the three hfs components is 1.8.

Table C.5: Hyperfine structure components of para-NH₃ 2₁ – 1₁.

Frequency ^a (MHz)	A_{ul} (s ⁻¹)	Δv^b (km s ⁻¹)	Rel. Intensity ^a $\frac{A_{ul} \times g_u}{A_{ul}(\text{main}) \times g_u(\text{main})}^c$
1215.2443	1.02e-2	0.31	0.536
1215.2449	3.39e-3	0.16	0.179
1215.2453	5.65e-3	0.06	0.179
1215.2456	1.36e-2	0	1.0
1215.2459	3.77e-4	-0.09	0.012
1215.2468	7.53e-3	-0.32	0.238

Notes. ^(a) Coudert & Roueff (2006, 2009). ^(b) The velocity offset from the strongest hfs component at 1215.2456 MHz. ^(c) The sum of the relative intensities of the six hfs components is 2.14.

Appendix D: Method II results

Table D.1: *Results from Method II^a*.

W49N									
v_{LSR} (km s^{-1})	$N(\text{NH})^b$ (cm^{-2})	$N(\text{o-NH}_2)^b$ (cm^{-2})	$N(\text{o-NH}_3)$ (cm^{-2})	$N(\text{CH})$ (cm^{-2})	NH/o-NH ₃	o-NH ₂ /o-NH ₃	$X(\text{NH})^c$	$X(\text{o-NH}_2)^c$	$X(\text{o-NH}_3)^c$
36.0 - 42.0	1.1e13	8.3e12	4.1e12	6.3e13	2.7	2.0	6.1e-9	4.6e-9	2.3e-9
50.0 - 57.0	1.4e12	1.4e12	1.2e12	6.6e13	1.2	1.2	7.4e-10	7.4e-10	6.4e-10
57.0 - 61.0	7.8e12	3.5e12	1.9e12	7.3e13	4.1	1.8	3.7e-9	1.7e-9	9.1e-10
61.0 - 70.0	1.0e13	4.8e12	3.0e12	9.1e13	3.3	1.6	3.8e-9	1.8e-9	1.2e-9
Total	3.0e13	1.8e13	1.0e13	2.9e14	3.0	1.8	3.6e-9	2.2e-9	1.2e-9
Mean	7.6e12	4.5e12	2.6e12	7.3e13	3.0	1.8	3.6e-9	2.2e-9	1.2e-9
Median	9.0e12	4.2e12	2.5e12	7.0e13	3.6	1.7	4.5e-9	2.1e-9	1.2e-9
G10.6-0.4									
v_{LSR} (km s^{-1})	$N(\text{NH})^b$ (cm^{-2})	$N(\text{o-NH}_2)^b$ (cm^{-2})	$N(\text{o-NH}_3)$ (cm^{-2})	$N(\text{CH})$ (cm^{-2})	NH/o-NH ₃	o-NH ₂ /o-NH ₃	$X(\text{NH})^c$	$X(\text{o-NH}_2)^c$	$X(\text{o-NH}_3)^c$
12.5 - 20.0	2.9e13	1.4e13	5.4e12	1.2e14	5.4	2.6	8.5e-9	4.1e-9	1.6e-9
20.0 - 25.0	2.7e13	1.2e13	3.8e12	9.3e13	7.1	3.2	1.0e-8	4.5e-9	1.4e-9
25.0 - 29.0	3.0e13	1.5e13	8.4e12	1.2e14	3.6	1.8	8.8e-9	4.4e-9	2.5e-9
29.0 - 31.0	2.8e13	1.2e13	6.9e12	5.4e13	4.1	1.7	1.8e-8	7.8e-9	4.5e-9
31.0 - 35.0	1.4e13	5.0e12	2.8e12	7.1e13	5.0	1.8	6.9e-9	2.5e-9	1.4e-9
35.0 - 39.5	2.6e13	8.2e12	3.0e12	1.1e14	8.7	2.7	8.3e-9	2.6e-9	9.6e-10
39.5 - 43.5	3.2e13	1.1e13	3.9e12	6.3e13	8.2	2.8	1.8e-8	6.1e-9	2.2e-9
43.5 - 50.0	1.8e12	1.0e12	8.0e11	1.9e13	2.3	1.3	3.3e-9	1.8e-9	1.5e-9
Total	1.9e14	7.8e13	3.5e13	6.5e14	5.4	2.2	1.0e-8	4.2e-9	1.9e-9
Mean	2.3e13	9.8e12	4.4e12	8.1e13	5.4	2.2	1.0e-8	4.2e-9	1.9e-9
Median	2.7e13	1.1e13	3.9e12	8.2e13	7.1	3.0	1.2e-8	4.9e-9	1.6e-9

Notes. ^(a) Column densities, $N(x)$, column density ratios, and abundances, $X(x) = N(x)/N(\text{H}_2)$, in different velocity ranges. ^(b) Using ortho-NH₃ 1₀-0₀ as a template. ^(c) Using $[\text{CH}]/[\text{H}_2] = 3.5 \times 10^{-8}$ (Sheffer et al. 2008).

Appendix E: Method III results

Table E.1: *Method III results^a*.

W49N										
v_{LSR} (km s ⁻¹)	Δv (km s ⁻¹)	$N(\text{NH})$ (cm ⁻²)	$N(\text{o-NH}_2)$ (cm ⁻²)	$N(\text{o-NH}_3)$ (cm ⁻²)	$N(\text{CH})$ (cm ⁻²)	NH/o-NH ₃	o-NH ₂ /o-NH ₃	$X(\text{NH})^b$	$X(\text{o-NH}_2)^b$	$X(\text{o-NH}_3)^b$
33.5	1.9	1.1e12	2.2e12	3.6e11	3.2e13	3.1	6.1	1.2e-9	2.4e-9	3.9e-10
39.6	1.1	1.2e13	7.4e12	3.2e12	3.3e13	3.8	2.3	1.3e-8	7.8e-9	3.4e-9
59.4	3.0	1.1e13	3.5e12	1.7e12	7.0e13	6.5	2.1	5.5e-9	1.8e-9	8.5e-10
62.8	2.4	9.7e12	3.2e12	1.9e12	5.8e13	5.1	1.7	5.9e-9	1.9e-9	1.1e-9
Total:	...	3.4e13	1.6e13	7.2e12	1.9e14	4.7	2.3	6.1e-9	3.0e-9	1.3e-9
Mean:	...	8.5e12	4.1e12	1.8e12	4.8e13	4.7	2.3	6.1e-9	3.0e-9	1.3e-9
Median:	...	1.0e13	3.4e12	1.8e12	4.6e13	5.8	1.9	8.0e-9	2.6e-9	1.4e-9
G10.6-0.4										
v_{LSR} (km s ⁻¹)	Δv (km s ⁻¹)	$N(\text{NH})$ (cm ⁻²)	$N(\text{o-NH}_2)$ (cm ⁻²)	$N(\text{o-NH}_3)$ (cm ⁻²)	$N(\text{CH})$ (cm ⁻²)	NH/o-NH ₃	o-NH ₂ /o-NH ₃	$X(\text{NH})^b$	$X(\text{o-NH}_2)^b$	$X(\text{o-NH}_3)^b$
tables 16.3	1.9	2.4e13	9.6e12	3.4e12	7.7e13	7.1	2.8	1.1e-8	4.4e-9	1.5e-9
19.0	1.3	6.8e12	2.3e12	6.0e11	2.6e13	11	3.8	9.2e-9	3.1e-9	8.1e-10
22.2	4.2	1.9e13	7.4e12	1.7e12	9.0e13	11	4.4	7.4e-9	2.9e-9	6.6e-10
22.9	1.0	1.1e13	3.0e12	1.0e12	1.2e13	11	3.0	3.2e-8	8.8e-9	2.9e-9
25.0	3.3	8.3e12	4.8e12	1.1e12	4.0e13	7.5	4.4	7.3e-9	4.2e-9	9.6e-10
28.0	1.9	3.2e13	1.2e13	6.4e12	9.8e13	5.0	1.9	1.1e-8	4.3e-9	2.3e-9
30.0	1.5	3.1e13	1.4e13	6.8e12	6.1e13	4.6	2.1	1.8e-8	8.0e-9	3.9e-9
32.2	1.7	1.2e13	3.1e12	8.9e11	2.5e13	13	3.5	1.7e-8	4.3e-9	1.2e-9
36.2	3.8	2.2e13	7.3e12	2.5e12	9.4e13	8.8	2.9	8.2e-9	2.7e-9	9.3e-10
39.1	1.2	1.4e13	3.2e12	5.5e11	4.6e13	25	5.8	1.1e-8	2.4e-9	4.2e-10
41.0	1.7	3.5e13	1.1e13	3.1e12	8.5e13	11	3.5	1.4e-8	4.5e-9	1.3e-9
45.1	1.3	3.7e12	1.6e12	3.8e11	1.4e13	9.7	4.2	9.3e-9	4.0e-9	9.5e-10
Total:	...	2.2e14	7.9e13	2.8e13	6.7e14	7.7	2.8	1.1e-8	4.2e-9	1.5e-9
Mean:	...	1.8e13	6.6e12	2.4e12	5.6e13	7.7	2.8	1.1e-8	4.2e-9	1.5e-9
Median:	...	1.7e13	6.1e12	1.4e12	5.4e13	12	4.3	1.1e-8	4.0e-9	9.2e-10

Notes. ^(a) LSR velocity, v_{LSR} , line width, Δv , column densities, $N(x)$, column density ratios and abundances, $X(x) = N(x)/N(\text{H}_2)$, of each velocity component. ^(b) $X(x) = N(x)/N(\text{H}_2)$ using $[\text{CH}]/[\text{H}_2] = 3.5 \times 10^{-8}$ (Sheffer et al. 2008).

Appendix F: Results for CN and HNC

Table F.1: *Method I and III results for CN and HNC^a*.

W49N		Method I				Method III			
v_{LSR} (km s ⁻¹)	Δv (km s ⁻¹)	$N(\text{CN})$ (cm ⁻²)	$N(\text{HNC})$ (cm ⁻²)	CN/o-NH ₃	HNC/o-NH ₃	$N(\text{CN})$ (cm ⁻²)	$N(\text{HNC})$ (cm ⁻²)	CN/o-NH ₃	HNC/o-NH ₃
33.5	1.9	8.1e12	4.3e11	18	0.93	7.5e12	4.5e11	21	1.3
39.6	1.1	6.6e13	2.9e12	15	0.67	6.3e13	2.9e12	20	0.91
59.4	3.0	3.5e13	2.1e12	17	1.0	3.3e13	2.2e12	19	1.3
62.8	2.4	2.8e13	1.5e12	13	0.68	2.6e13	1.7e12	14	0.89
Total:		1.4e14	6.9e12	15	0.76	1.3e14	7.3e12	18	1.0
Mean:		3.4e13	1.7e12	15	0.76	3.2e13	1.8e12	18	1.0
Median:		3.2e13	1.8e12	15	0.84	3.0e13	2.0e12	16	1.1

G10.6-0.4		Method I				Method III			
v_{LSR} (km s ⁻¹)	Δv (km s ⁻¹)	$N(\text{CN})$ (cm ⁻²)	$N(\text{HNC})$ (cm ⁻²)	CN/o-NH ₃	HNC/o-NH ₃	$N(\text{CN})$ (cm ⁻²)	$N(\text{HNC})$ (cm ⁻²)	CN/o-NH ₃	HNC/o-NH ₃
16.3	1.9	1.0e14	3.6e12	24	0.86	9.0e13	4.1e12	26	1.2
19.0	1.3	3.3e13	1.3e12	38	1.5	2.9e13	1.5e12	48	2.5
22.2	4.2	5.7e13	2.7e12	32	1.5	5.1e13	3.1e12	30	1.8
22.9	1.0	6.6e13	2.5e12	44	1.7	5.8e13	2.9e12	58	2.9
25.0	3.3	9.5e12	...	6.8	...	8.4e12	1.7e12	7.6	1.5
28.0	1.9	1.2e14	4.1e12	16	0.56	1.1e14	4.7e12	17	0.73
30.0	1.5	1.4e14	5.8e12	18	0.73	1.3e14	6.7e12	19	1.0
32.2	1.7	2.5e13	1.0e12	19	0.77	2.3e13	1.2e12	26	1.3
36.2	3.8	1.0e14	5.1e12	31	1.6	9.0e13	5.9e12	36	2.4
39.1	1.2	3.7e13	1.1e12	79	2.3	3.3e13	1.3e12	60	2.4
41.0	1.7	1.6e14	5.9e12	39	1.4	1.4e14	6.8e12	45	2.2
45.1	1.3	1.2e13	8.5e11	20	1.4	1.1e14	9.7e12	289	26
Total:		8.6e14	3.4e13	25	1.0	8.7e14	5.0e13	31	1.7
Mean:		7.2e13	3.1e12	25	1.0	7.4e13	3.6e12	53	2.6
Median:		6.2e13	2.7e12	37	1.5	7.3e13	4.1e12	31	1.7

Notes. ^(a) LSR velocity, v_{LSR} , line width, Δv , and column densities, N , of each velocity component, and column density ratios.

Table F.2: *CN and HNC results from Method II^a.*

W49N				
v_{LSR} (km s ⁻¹)	$N(\text{CN})^b$ (cm ⁻²)	$N(\text{HNC})^b$ (cm ⁻²)	CN/o-NH ₃	HNC/o-NH ₃
36.0 - 42.0	5.3e13	2.9e12	13	0.71
50.0 - 57.0	4.4e12	5.7e11	3.7	0.48
57.0 - 61.0	2.1e13	1.7e12	11	0.89
61.0 - 70.0	2.6e13	2.0e12	8.7	0.67
Total	1.0e14	7.2e12	10	0.70
Mean	2.6e13	1.8e12	10	0.70
Median	2.4e13	1.9e12	9.6	0.76
G10.6-0.4				
v_{LSR} (km s ⁻¹)	$N(\text{CN})^b$ (cm ⁻²)	$N(\text{HNC})^b$ (cm ⁻²)	CN/o-NH ₃	HNC/o-NH ₃
12.5 - 20.0	1.0e14	5.8e12	19	1.1
20.0 - 25.0	9.1e13	5.2e12	24	1.4
25.0 - 29.0	9.6e13	5.6e12	11	0.67
29.0 - 31.0	8.8e13	4.9e12	13	0.71
31.0 - 35.0	4.2e13	2.3e12	15	0.82
35.0 - 39.5	8.0e13	5.3e12	27	1.8
39.5 - 43.5	1.4e14	7.4e12	36	1.9
43.5 - 50.0	9.8e12	1.1e12	12	1.4
Total	6.5e14	3.8e13	18	1.1
Mean	8.1e13	4.7e12	18	1.1
Median	9.0e13	5.3e12	23	1.4

Notes. ^(a) Column densities and ratios in different velocity ranges. ^(b) Using ortho-NH₃ 1₀ - 0₀ as a template.

Appendix G: Figures

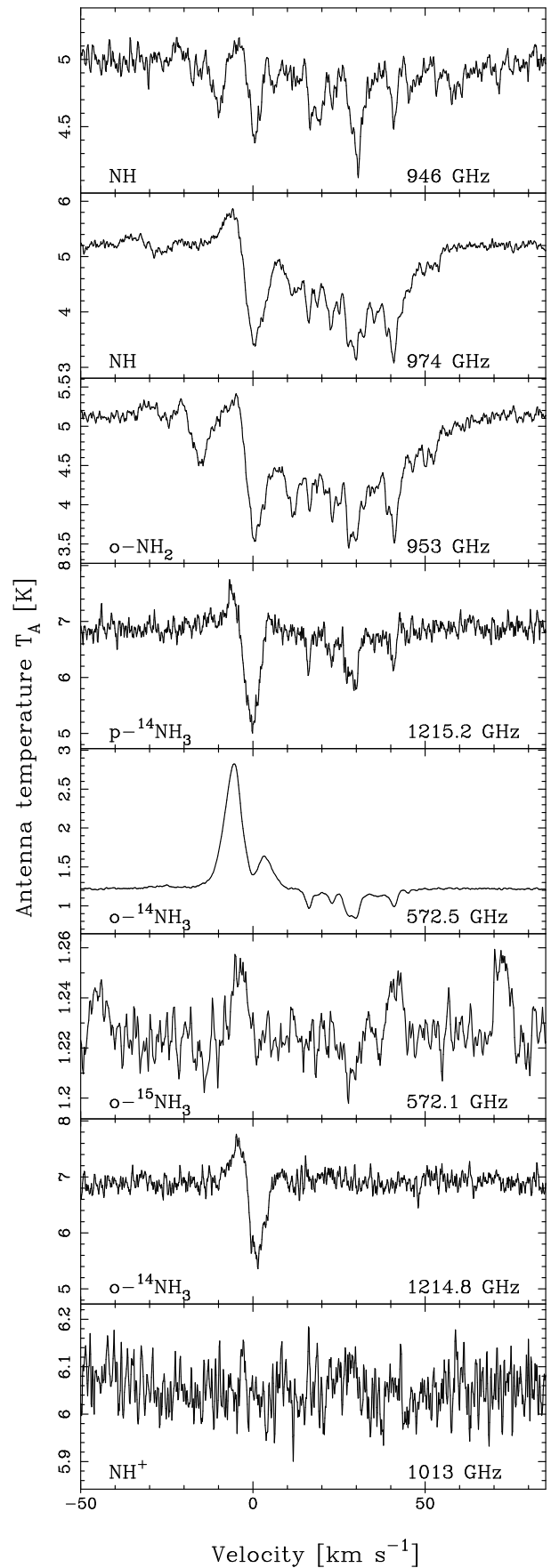


Fig. G.1: *G10.6-0.4 (W31C)*: Double sideband spectra of NH, ortho-NH₂, ortho- and para-¹⁴NH₃, ortho-¹⁵NH₃, and NH⁺ over the LSR velocity range -50 to 85 km s⁻¹.

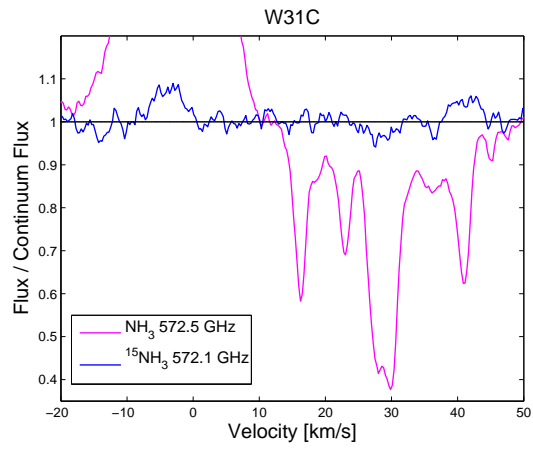


Fig. G.2: *G10.6-0.4* (W31C): Normalised ammonia and the ammonia isotopologue $^{15}\text{NH}_3$. (The emission line at $v_{\text{LSR}} \approx 41$ and 72 km s^{-1} is an SO_2 line from the upper sideband.)

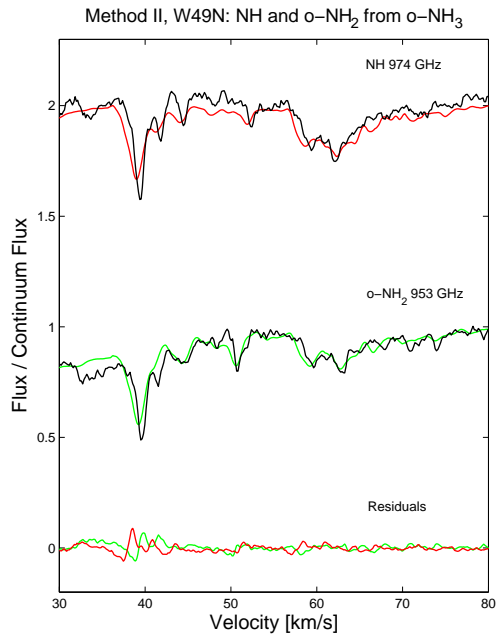


Fig. G.3: *W49N*: Fits of method II to NH and o-NH₂, and their observed spectra. Residuals are found at the bottom. Template spectrum is o-NH₃ at 572 GHz.

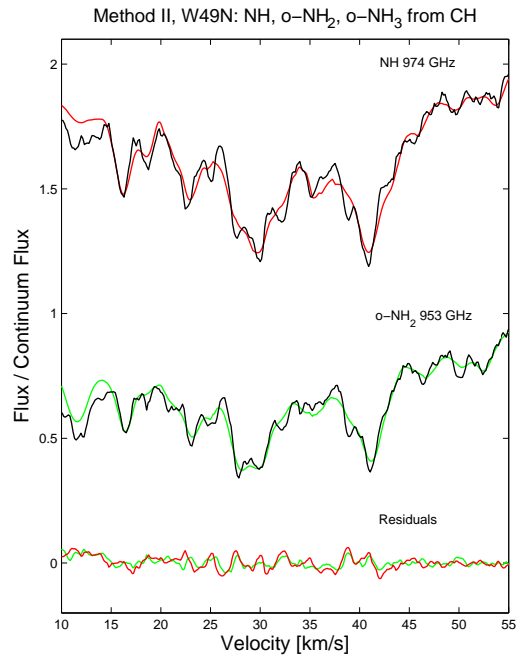


Fig. G.5: *G10.6-0.4 (W31C)*: Fits of method II to NH and o-NH₂, and their observed spectra. Residuals are found at the bottom. Template spectrum is o-NH₃ at 572 GHz.

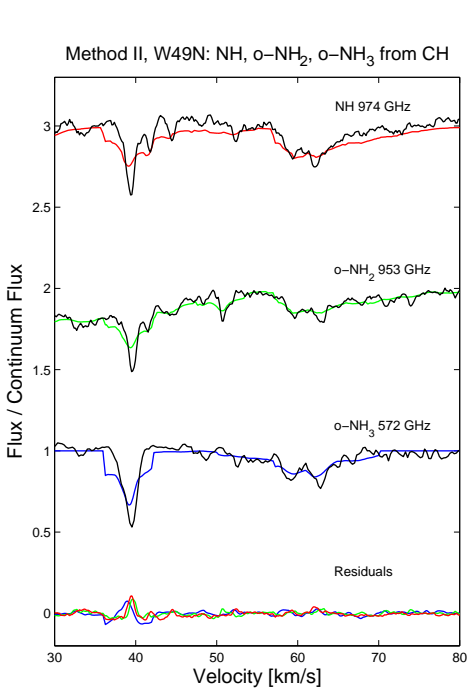


Fig. G.4: *W49N*: Fits of method II to NH, o-NH₂ and o-NH₃, and their observed spectra. Residuals are found at the bottom. Template spectrum is CH at 532 GHz.

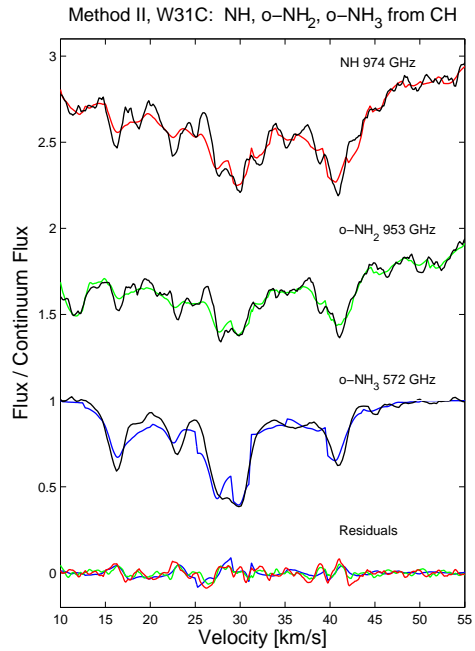


Fig. G.6: *G10.6-0.4 (W31C)*: Fits of method II to NH, o-NH₂ and o-NH₃, and their observed spectra. Residuals are found at the bottom. Template spectrum is CH at 532 GHz.

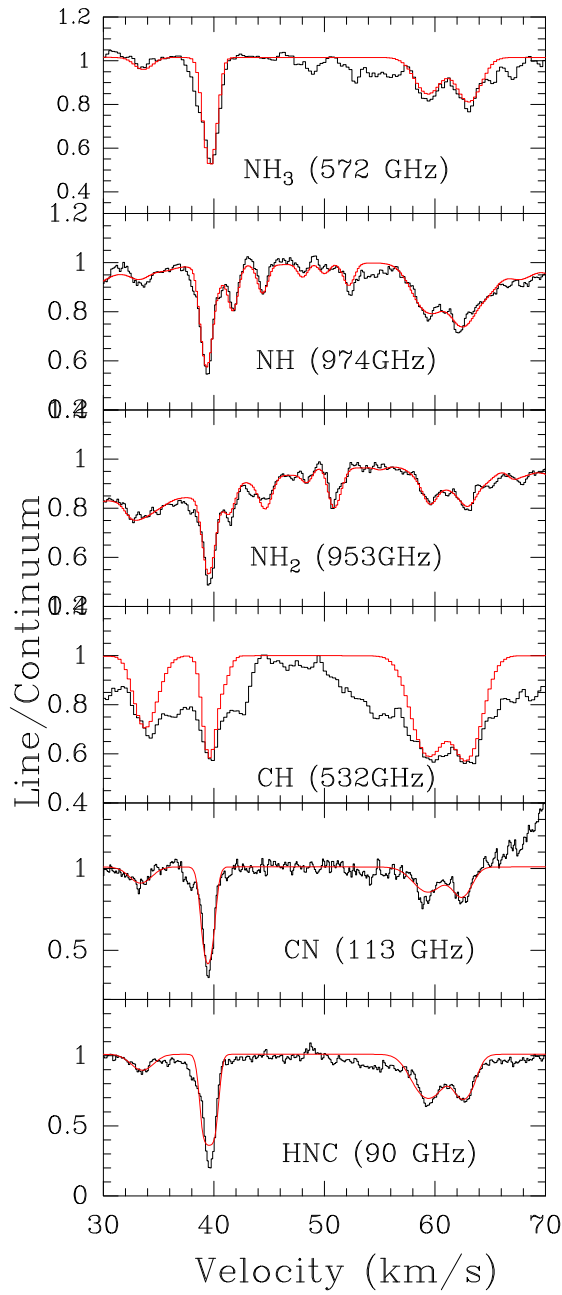


Fig. G.7: *W49N*: Method III (XCLASS) fits to the Nitrogen hydrides and CH.

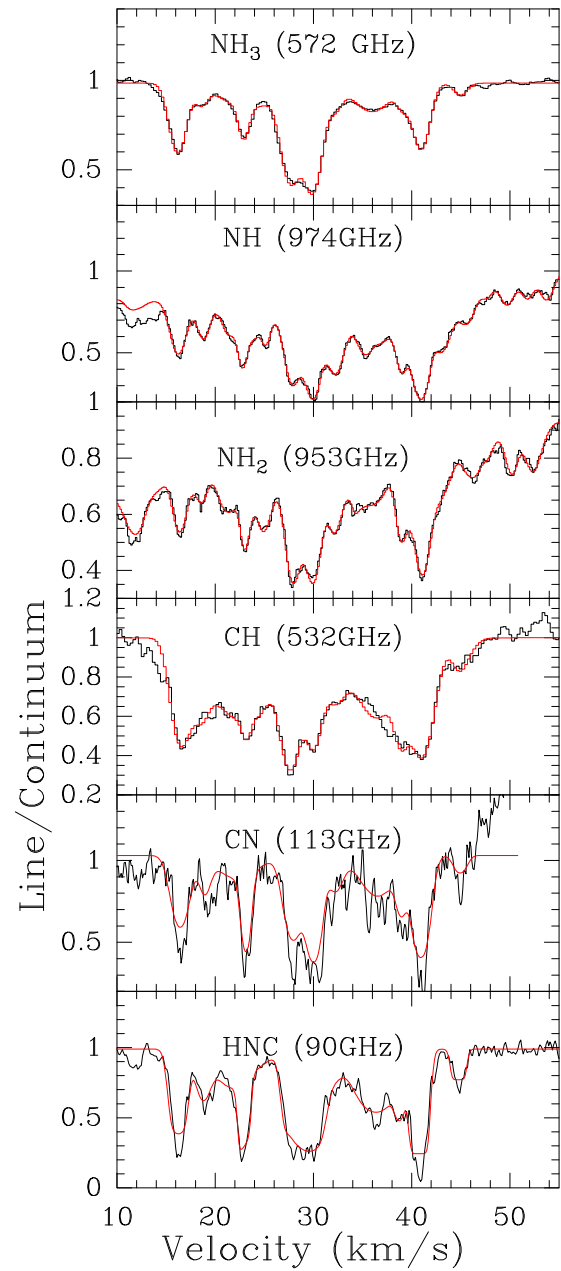


Fig. G.8: *G10.6-0.4 (W31C)*: Method III (XCLASS) fits to the Nitrogen hydrides and CH.

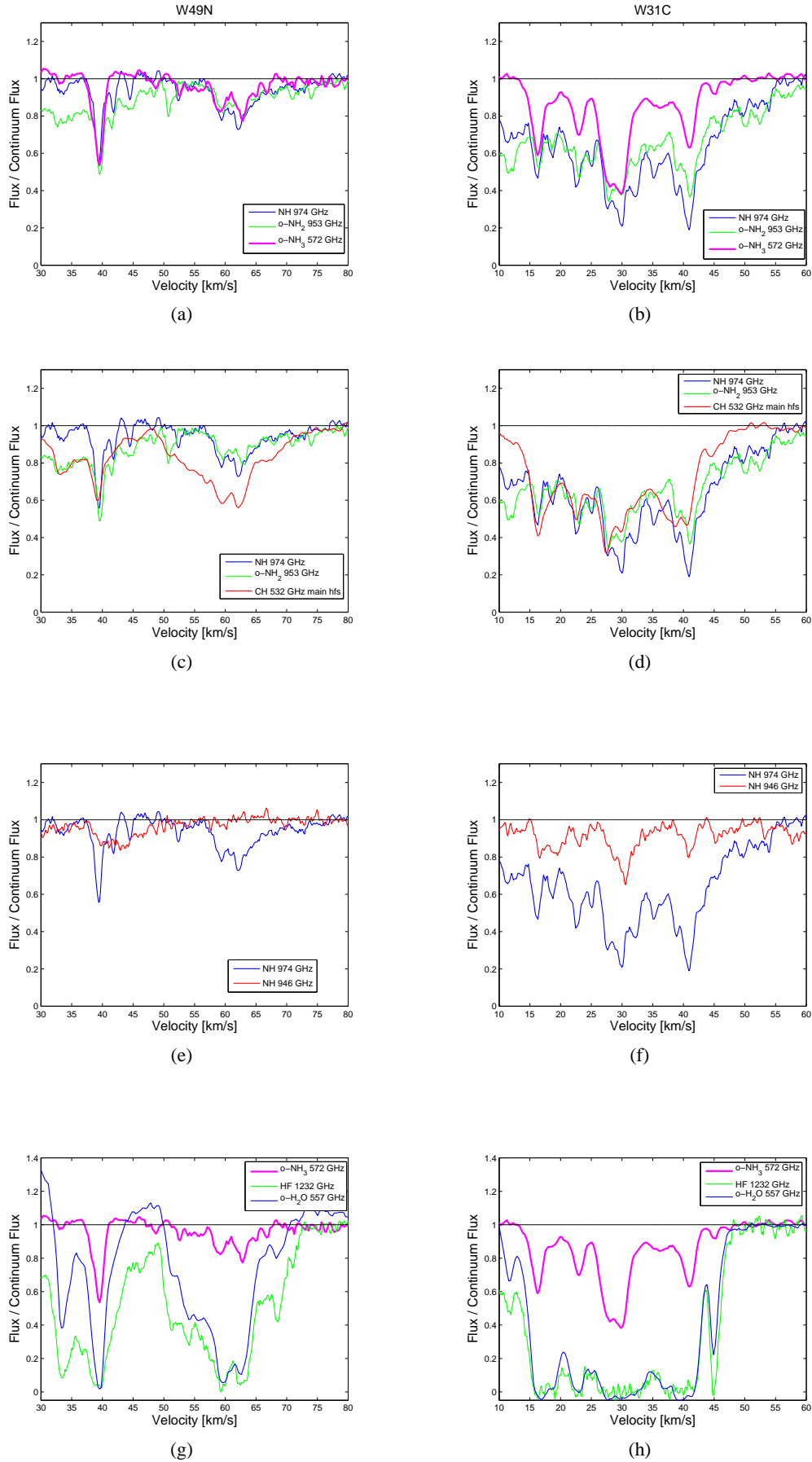


Fig. G.9: Comparison of absorption lines towards W49N and G10.6-0.4. The intensities have been normalised to single sideband continuum. An NO emission line from the source (952.464 GHz) has been removed from the o-NH₂ spectrum (see Sect. B.).

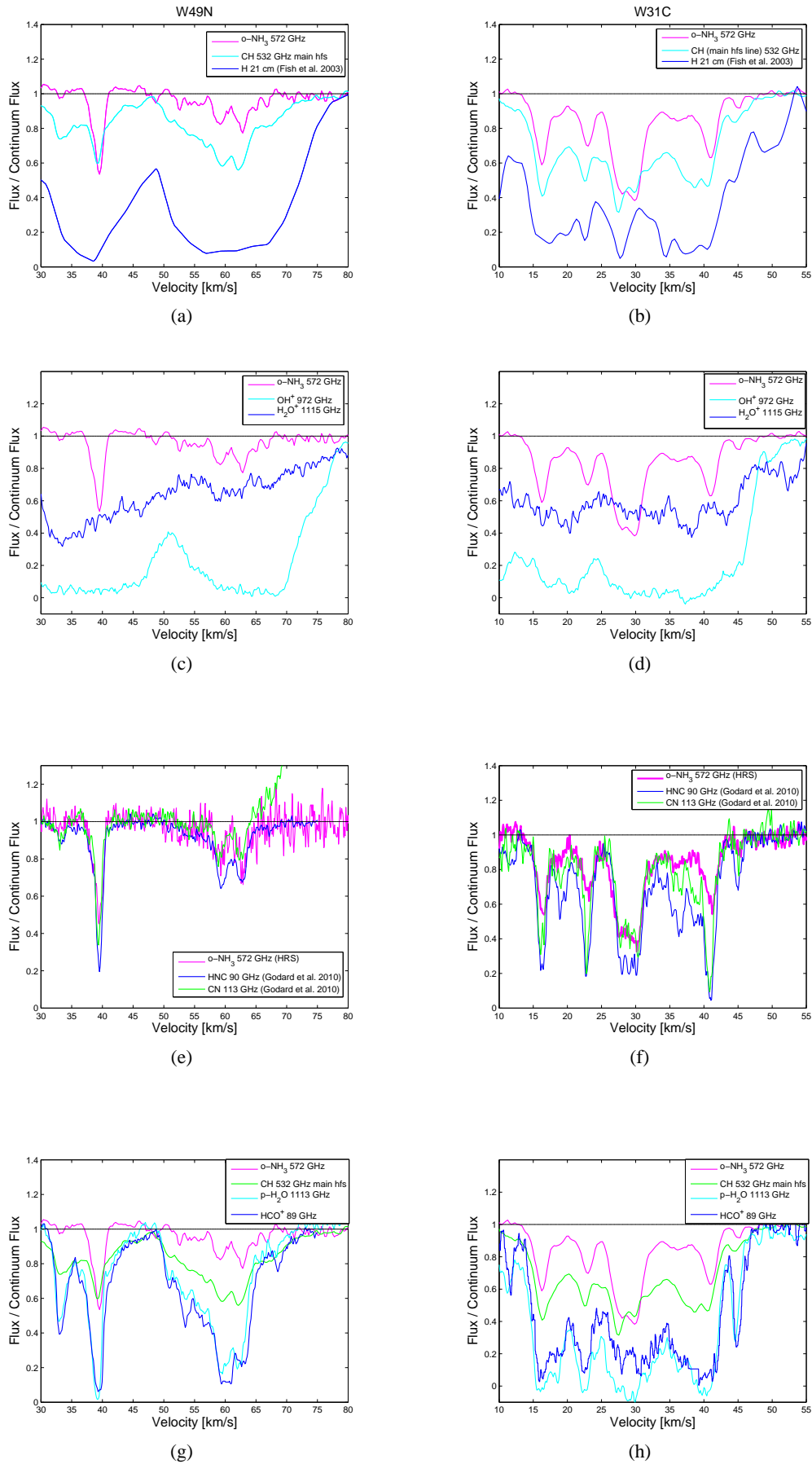


Fig. G.10: Comparison of absorption lines towards W49N and G10.6–0.4. The intensities have been normalised to single sideband continuum.

Appendix H: Comparison plots of different methods

In Figs. H.1–H.4 we plot the resulting column densities from our three different methods.

Note that since Method I and Method III use Gaussians with smaller line widths than the velocity bins of Method II towards G10.6–0.4, the number of velocity components is not the same in this source. The $+33 \text{ km s}^{-1}$ component towards W49N is not used in Method II, which on the other hand models a velocity bin that is difficult to fit using Gaussians in Method I and III ($50–57 \text{ km s}^{-1}$). The comparison of the nitrogen hydrides vs. CH in W49N, in two of the four velocity bins, shows the only cases in which the results do not agree reasonably well between the methods. The resulting CH column densities also show a larger spread between the methods than the other species. The reason is not fully understood, but is probably caused by the different approaches to the CH modelling. Method II uses the deconvolved CH spectra as a template for the nitrogen hydrides and is thereby trying to fit the broader CH absorption to the more narrow features of the nitrogen hydrides with moderate success. The other two methods use an opposite approach: they use the output of the fitting of the nitrogen hydrides as an input to CH to fit Gaussians only in the same parts in velocity space, and are thereby trying to fit narrow features to the broader CH absorption. The fit is good in some parts of the velocity space, and very bad in the velocity space in which CH has absorption but the nitrogen hydrides do not, which is expected.

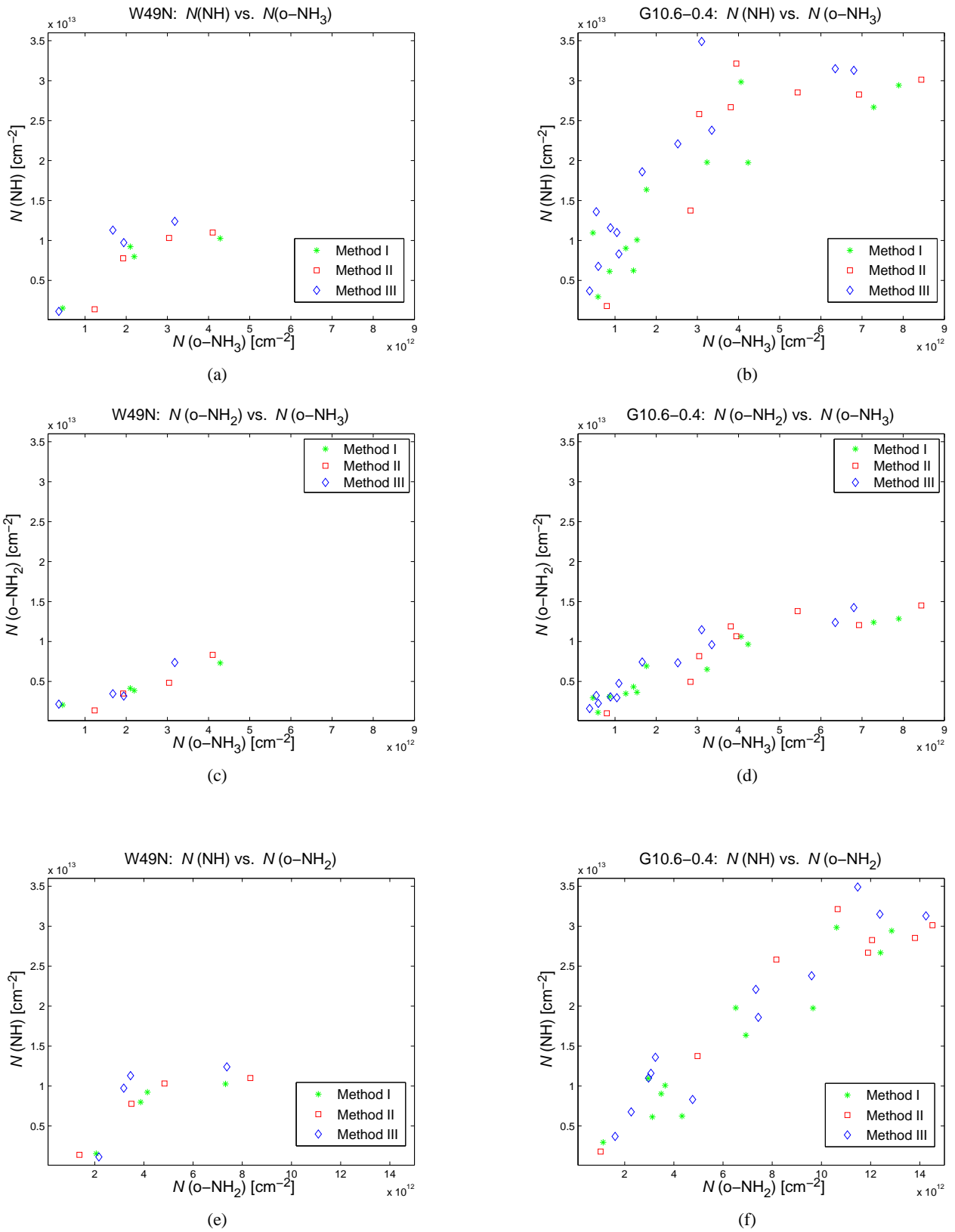


Fig. H.1: Column density comparison plots. The results from all three methods are plotted. The scatter in the results can be considered as an estimate of the errors.

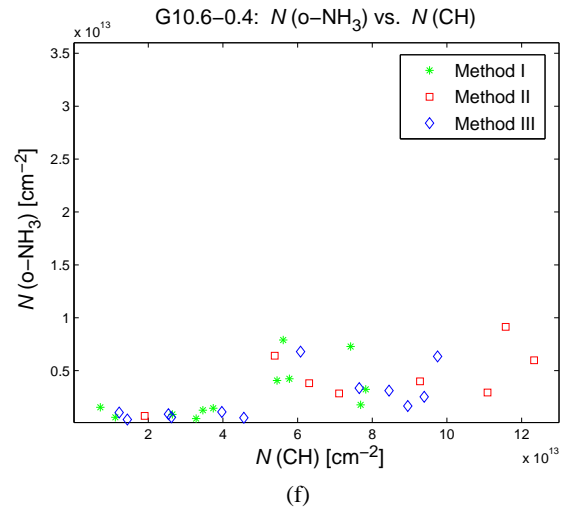
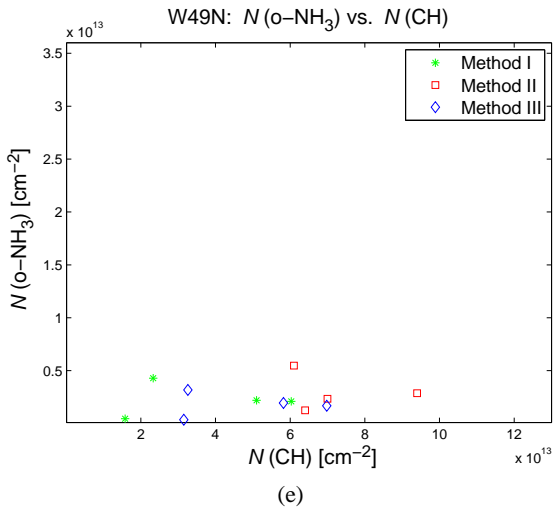
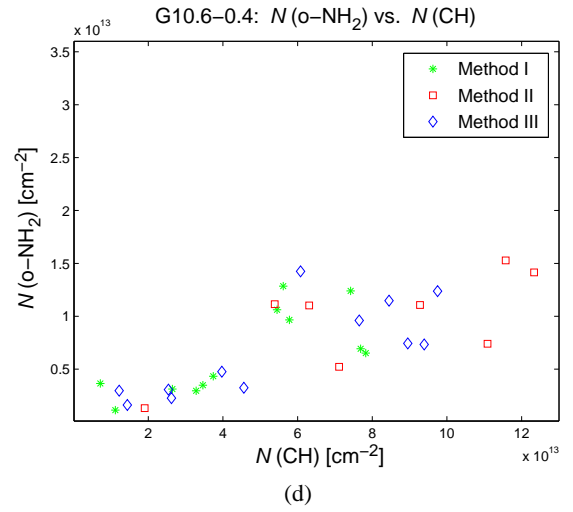
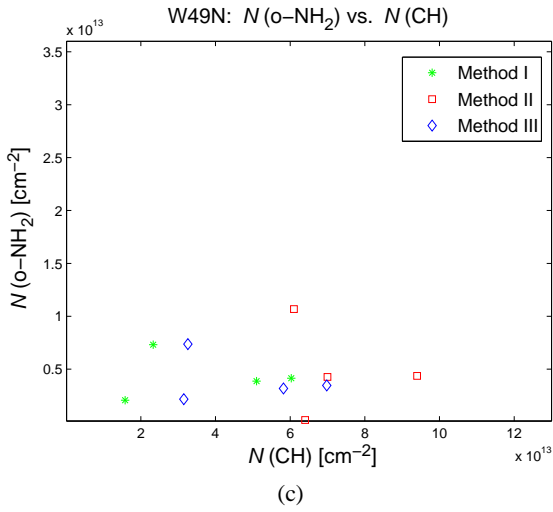
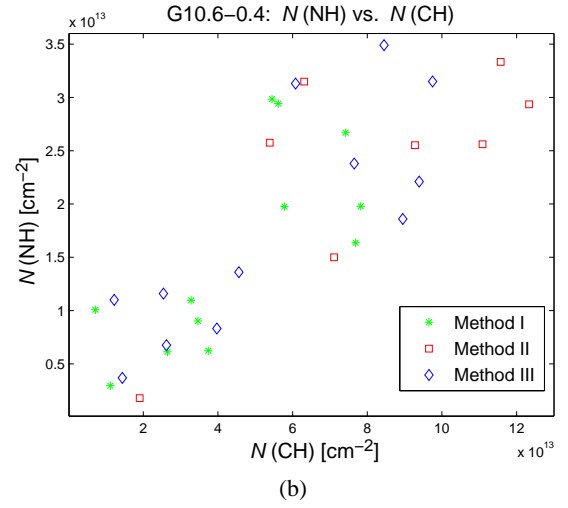
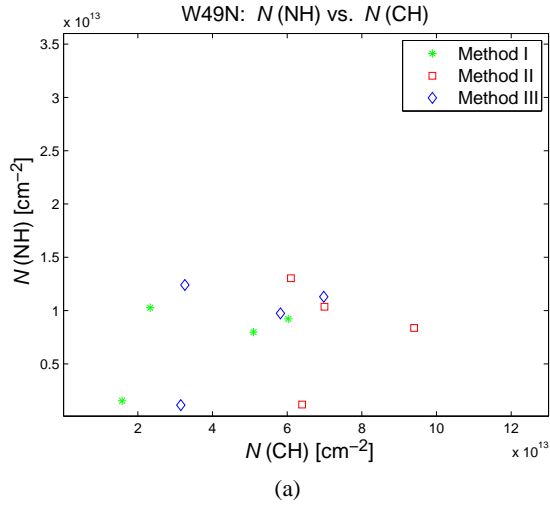


Fig. H.2: *Cont: Column density comparison plots 2. Notation as in Fig. H.1.*

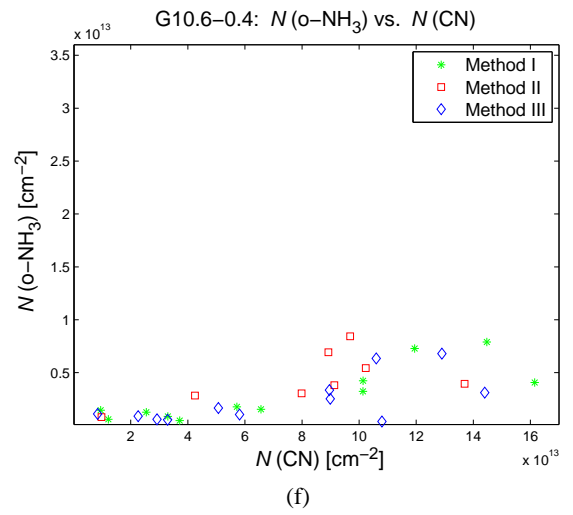
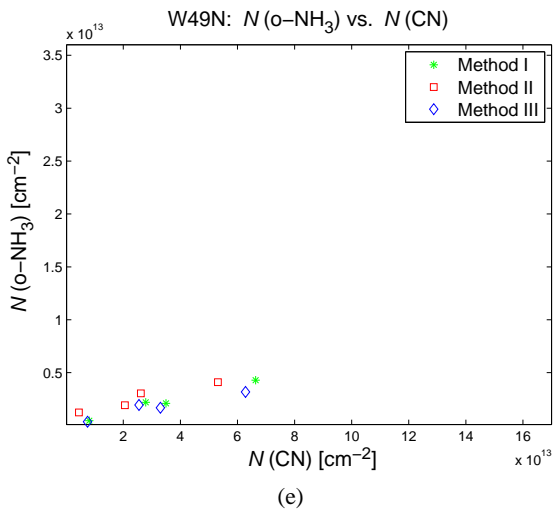
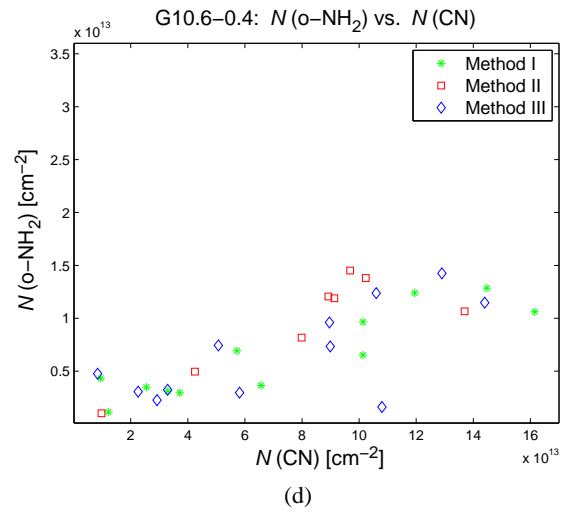
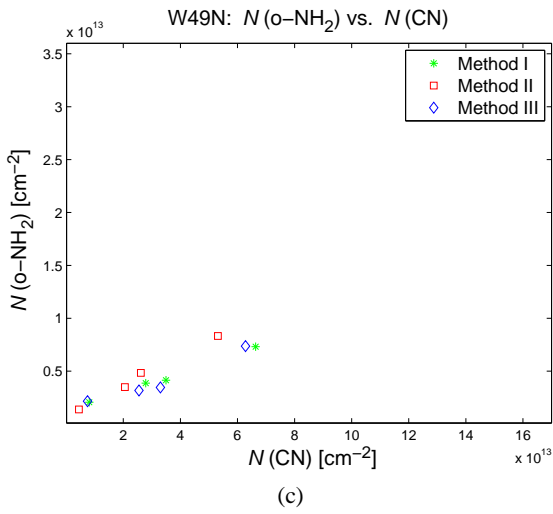
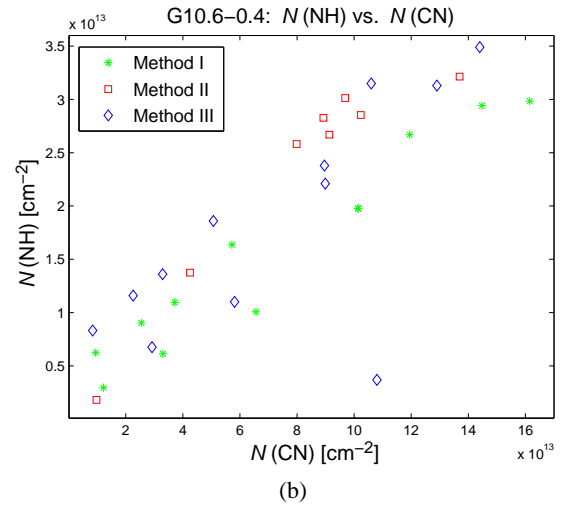
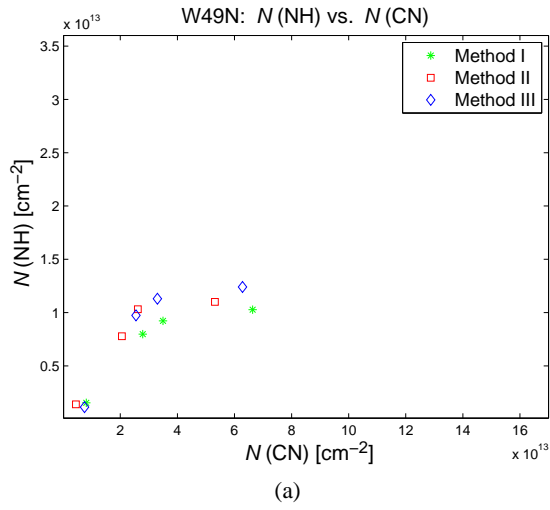


Fig. H.3: *Cont*: Column density comparison plots 3. Notation as in Fig. H.1.

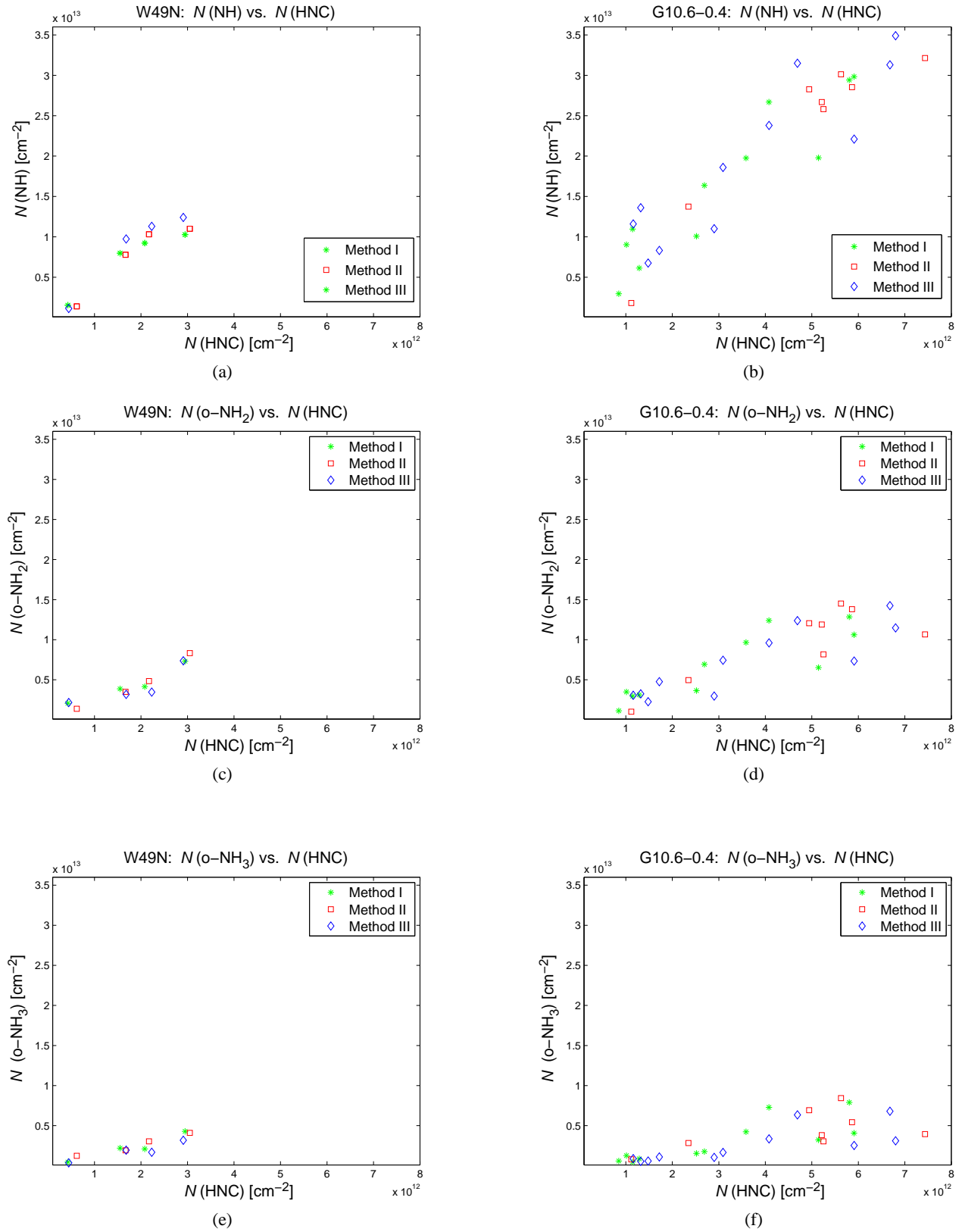


Fig. H.4: *Cont: Column density comparison plots 4. Notation as in Fig. H.1.*